Yaw Rate and Lateral Acceleration Sensor Plausibilisation in an Active Front Steering Vehicle

Master's thesis
performed in **Vehicular Systems**
for **ZF Lenksysteme**

by
Anders Wikström

Reg nr: LiTH-ISY-EX -- 06/3818 -- SE

November 9, 2006

Yaw Rate and Lateral Acceleration Sensor Plausibilisation in an Active Front Steering Vehicle

Master's thesis

performed in **Vehicular Systems**,
Dept. of Electrical Engineering
at **Linköpings universitet**

by **Anders Wikström**

Reg nr: LiTH-ISY-EX -- 06/3818 -- SE

Supervisors: **Samuel Malinen**
ZF Lenksysteme
Jonas Biteus
Linköpings Universitet

Examiner: **Assistant Professor Erik Frisk**
Linköpings Universitet

Linköping, November 9, 2006

Abstract

Accurate measurements from sensors measuring the vehicle's lateral behavior are vital in todays vehicle dynamic control systems such as the Electronic Stability Program (ESP). This thesis concerns accurate plausibilisation of two of these sensors, namely the yaw rate sensor and the lateral acceleration sensor. The estimation is based on Kalman filtering and culminates in the use of a 2 degree-of-freedom nonlinear two-track model describing the vehicle lateral dynamics. The unknown and time-varying cornering stiffnesses are adapted and other unknown quantities such as yaw moment of inertia is estimated. The Kalman filter transforms the measured signals into a sequence of residuals that are then investigated with the aid of various change detection methods such as the CuSum algorithm. An investigation into the area of adaptive thresholding has also been made.

The change detection methods investigated successfully detects faults in both the yaw rate and the lateral acceleration sensor. It it also shown that adaptive thresholding can be used to improve the diagnosis system. All of the results have been evaluated on-line in a prototype vehicle with real-time fault injection.

Keywords: Yaw rate, Lateral acceleration, Diagnosis, Change detection, Bicycle model

Preface

This master's thesis has been performed at the EEMF-department at ZF Lenksysteme GmbH in Schwäbisch Gmünd, Germany, during the first half of 2006.

Thesis outline

Chapter 1 - Introduction The first chapter gives a short introduction to the background and the objectives of this thesis.

Chapter 2 - Vehicle modeling Concerns the derivation of the vehicle models investigated. This chapter also contains the estimation and adaptation of the involved parameters.

Chapter 3 - Observer theory Contains the necessary observer theory and observer design issues.

Chapter 4 - Kinematic relations Contains the derivation of different kinematic relations.

Chapter 5 - Change detection This chapter investigates different methods of change detection and their possibility to improve the performance of the diagnosis system.

Chapter 6 - Results The results achieved are presented in this chapter.

Chapter 7 - Conclusions and future work Contains the conclusions drawn from this thesis and suggestions for future work.

Acknowledgment

First I would like to thank my supervisors at ZF Lenksysteme, Samuel Malinen and Wolfgang Reinelt for all their help during the writing of this thesis. I am also very grateful for the feedback and comments provided by Jonas Biteus who has been my supervisor at Linköpings Universitet. Furthermore, thanks to all the people at the EEMF-department and all the other people I got in contact with during my stay in Schwäbisch Gmünd. You all made my stay there more enjoyable!

Anders Wikström
Schwäbisch Gmünd, June 2006

Notation

Variables and parameters

Symbol	Description	Unit
AFS System		
δ_G	Pinion angle	rad
δ_S	Steering wheel angle	rad
δ_M	Motor angle	rad
i_M	Motor angle to pinion angle ratio	-
i_D	Steering wheel angle to pinion angle ratio	-
F_{SG}	Pinion angle to rack displacement static nonlinearity	-
Vehicle model		
$\delta_F, \delta_{F,mid}$	Road wheel angle	rad
$\delta_{F,d}$	Delayed Road wheel angle	rad
m	Vehicle mass	kg
l_r	Distance from CoG to rear axle	m
l_f	Distance from CoG to front axle	m
l	Distance from rear axle to front axle	m
S_f	Front track width	m
S_r	Rear track width	m
S_{av}	Average track width	m
I_z	Yaw moment of inertia	kgm^2
$C_{\alpha,r}$	Rear cornering stiffness	N/rad
$C_{\alpha,f}$	Front cornering stiffness	N/rad
v_x	Longitudinal velocity	m/s
v_y	Lateral velocity	m/s
v	Vehicle velocity	m/s
v_{ij}	Velocity on wheel *ij*	m/s
a_x	Longitudinal acceleration	m/s^2
a_y	Lateral acceleration	m/s^2
β	Sideslip angle	rad
$\dot{\Psi}$	Yaw rate	rad/s
α_i	Slip angle on wheel *i*	rad
$F_{y,ij}$	Lateral wheel force on tire *ij*	N
$F_{z,ij}$	Vertical wheel force on tire *ij*	N
M_z	Torque around the z-axis	Nm
g	Universal gravitational constant	m/s^2
h_{cog}	Center of gravity height	m
a_{ij}, b_{ij}, c_{ij}	Lateral force parameters	-
S	Quality function	-

Symbol	Description
Kalman filter	
w	Process noise
v	Measurement noise
K	Kalman gain
Q	Process noise covariance
R	Measurement noise covariance
P	Error covariance
Change detection	
r_t	Residual
s_t	Distance measure
g_t	Test statistic
W	Model uncertainty measure
J	Threshold
J_{adp}	Adaptive threshold
p_θ	Probability density
ν	CuSum drift parameter
h	CuSum threshold parameter

Acronyms

AFS	Active Front Steering
CoG	Center of Gravity
CuSum	Cumulative Sum
ECU	Electronic Control Unit
EKF	Extended Kalman Filter
ESP	Electronic Steering Program
ISO	International Organization for Standardization
VDC	Vehicle Dynamics Control
YRS	Yaw Rate Sensor
ZF	Zahnrad Fabrik (Cogwheel Factory)

Contents

Chapter 1

Introduction

1.1 Background

During the last decade, Vehicle Dynamics Control (VDC) systems, such as the Electronic Stability Program (ESP), have been introduced and are now standard in most modern vehicles. These systems are created to help drivers in various driving situations where they otherwise would have lost control of the vehicle. For instance, ESP can help braking on individual wheels if the vehicle becomes uncontrollable for the driver and thus help the driver regain control of the vehicle. The VDC systems rely heavily on accurate measurements from the associated vehicle sensors and the monitoring of these sensors has been, and still is, an area of extensive research. The activation of lateral dynamics control of ESP relies on the yaw rate sensor signal and the lateral accelerometer sensor signal and accurate on-line monitoring and fault detection of these two sensors are the aim of this thesis.

1.2 Objective

The objective of this thesis can be divided into two parts. The first part is to design a monitoring function that detects failures in the yaw rate sensor. The second part is to design a monitoring function that detects failures in the lateral accelerometer sensor. Both functions are to be implemented as Simulink models and tested and validated on-line in a prototype vehicle at a proving ground and with real-time fault injection.

1.3 Active Front Steering

The German company ZF Lenksysteme GmbH has developed and patented a concept for Active Front Steering (AFS) which is a recently developed technology that superimposes an electronically controlled angle to the, by the driver prescribed, steering wheel angle. This is done while maintaining the mechanical coupling between steering wheel and front axle. The AFS-system basically consists of a rack and pinion hydraulic steering gear, an electric motor, some sensors and an Electronic Control Unit (ECU). The ingoing parts can be seen in Figure 1.1. The purpose of the AFS-system is to increase the comfort, ease of handling, and active safety for the driver. Depending on the driving situation, the effective angle between the road and the wheels will be either smaller or larger than that adjusted at the steering wheel by the driver. The ratio depends on vehicle velocity as well as pinion and steering wheel angle. At low velocities, the electric motor will add an angle to the steering wheel angle and thus making the steering more direct, which in turn increases the agility of the vehicle when performing maneuvers such as parking or driving in city traffic. Similarly, at high speeds, the electric motor intervenes and deducts an angle from the steering wheel angle, making the steering less direct. This reduces the risk for the driver losing control of the vehicle since, during normal driving conditions, large sudden steering wheel angles are not desirable when driving in high velocities.

The principle by which the AFS-system operates as well as all three angles of interest can be seen in Figure 1.2. The angle δ_S represents the steering wheel angle controlled by the driver, δ_M represents the electronically controlled motor angle that superimposed together with δ_S results in the pinion angle δ_G down at the steering rack. The relation between these angles is

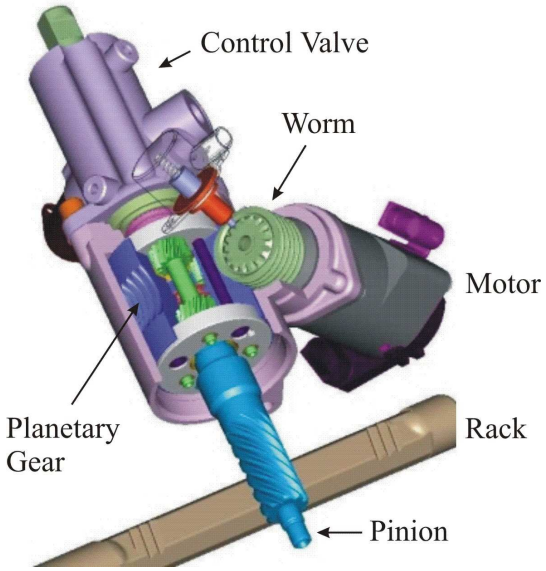

Figure 1.1: Overview of the AFS motor mechanism.

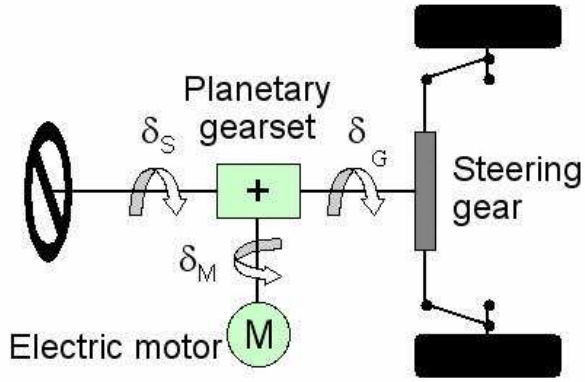

Figure 1.2: The AFS principle. An electronically controlled angle δ_M is superimposed to the steering wheel angle δ_S resulting in the pinion angle δ_G.

$$\delta_G(t) = \frac{1}{i_M}\delta_M(t) + \frac{1}{i_D}\delta_S(t) \tag{1.1}$$

where i_D and i_M account for the respective ratios. The resulting average road wheel angle δ_F can be calculated via

$$\delta_G(t) = F_{SG}(\delta_F(t)) \tag{1.2}$$

where $F_{SG}(\cdot)$ accounts for the relation between pinion angle and rack displacement as well as for the steering geometry (1.2).

1.4 Measurements

A large amount of measured data has been gathered and investigated during the writing of this thesis. The measurements have been performed partly at ZF Lenksysteme in Schwäbisch Gmünd, Germany, and partly in the proving grounds located in Arjeplog, Sweden. In the later stage of the thesis period, measurements were also collected from Boschs proving ground in Boxberg, Germany. A measurement schedule has been established and

therein, driving maneuvers were defined. The measurement vehicle used is a BMW-545i, equipped with the same sensors that appear in the commercial vehicle. Of particular interest is the Yaw Rate Sensor, YRS-MM1.1, that has been developed by Bosch GmbH. The sensor consists of two different measuring elements, one for measuring the yaw rate and one for measuring the lateral acceleration of the vehicle.

For the purpose of parameter estimation and validation, measured data from another BMW-545i equipped with extra sensors has been used. These extra sensors realizes measurements of the forces acting on each tyre in three dimensions as well as measurements of the vehicle's lateral velocity.

1.5 Contributions

When developing the vehicle models inspiration has been taken from other works that involves studies of simpler, both linear and nonlinear, vehicle models. However in order to get the most out of the diagnosis system a more accurate model of the vehicle's lateral dynamics was required and this resulted in the nonlinear model presented in this thesis. A well-balanced model that is accurate enough for the purpose of fault detection and at the same time not too complex.

This thesis also shows the successful application of various change detection methods in order to detect faults in the lateral acceleration and yaw rate sensors. Especially the use of adaptive thresholding in vehicle diagnosis systems is an area that is still fairly undeveloped. This thesis successfully shows how the diagnosis system can be improved by using adaptive thresholds.

While many works are purely theoretical, all work presented in this thesis has also been validated on-line in a prototype vehicle.

1.6 Related work

The areas of vehicle modeling and change detection are fairly well investigated. Numerous vehicle models of varying complexity have been developed and used in applications such as signal estimation. *"Sensor Fusion for Accurate Computation of Yaw Rate and Absolute Velocity"* by F. Gustafsson is one work that shows that sensor fusion can be used in order to accurately estimate the yaw rate and absolute velocity of a vehicle. Another related work is *"Observation of Lateral Vehicle Dynamics"* by U. Kiencke and A. Daiss that presents a comparison of a linear and a nonlinear observer for vehicle and tyre side-slip angles. The Ph.D thesis *"Model Based Detection and Reconstruction of Road Traffic Accidents"* by M. Hiemer presents a model based system for detection of road traffic accidents. The cornering stiffness adaptation procedure presented in this thesis is largely the same as in Hiemers work. Even though the applications are different in the end both works rely on an accurate and at the same time not too complex vehicle model.

Change detection or fault detection is also a very active field and this work has taken inspiration from *"AFS Change Detection Using Signal Estimation"* by Samuel Malinen which is a master thesis performed at ZF Lenksysteme that investigates the use of change detection in an Active Front Steering vehicle.

Chapter 2

Vehicle modeling

To accurately describe the vehicle dynamics an appropriate vehicle model must be derived. Since the purpose of this thesis is to monitor yaw rate and lateral acceleration the modeling of the vehicle lateral dynamics has been emphasized. First the well-known single-track model, also denoted bicycle model, is derived and the important tyre parameter called cornering stiffness is estimated. Next an extension of this model is made and the final nonlinear two-track model is derived. The two-track model furthermore includes the effects of load transfer as well as a more realistic nonlinear tyre model. Both models have been implemented in Simulink and evaluated on-line in a prototype vehicle with real-time fault injection.

2.1 Linear single-track model

A first approach involves the study of the linear single track model also denoted bicycle model. It is so called since the right and left wheel on both axis have been lumped together and the result can be seen in Figure 2.1. In Figure 2.1, $F_{y,f}$ and $F_{y,r}$ represent the lateral forces acting on the front and rear tyres respectively. Here and throughout this thesis, index f and r refer to the front and rear axis. The angles α_f and α_r are the slip angles on the front and rear wheel respectively and are defined as the difference between a wheel's direction of heading and its direction of travel. The variables v_x and v_y represent the vehicle's longitudinal and lateral velocities at the center of gravity (CoG). The angle δ_F is the road wheel angle for the front wheel and β represent the vehicle body side slip angle. Finally $\dot{\Psi}$ represents the yaw rate around the vehicle's CoG.

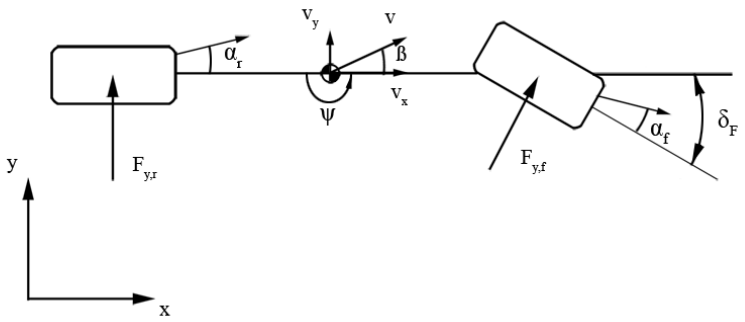

Figure 2.1: The linear bicycle model.

Since this model lumps the wheels on each axis together, equal slip angles and road wheel angles are assumed on the left and right wheels on both axis. The tyres are assumed to generate lateral forces that are directly proportional to the tyre slip angle [6],[9]. Hence the lateral forces are modeled as

$$F_{y,f} = C_{\alpha,f}\alpha_f \tag{2.1}$$
$$F_{y,r} = C_{\alpha,r}\alpha_r \tag{2.2}$$

where $C_{\alpha i}$, for $i \in \{f, r\}$, represent the cornering stiffnesses on each axis, which here equals two times the cornering stiffness on each wheel, and is defined as the slope of the curve seen in Figure 2.5 at $\alpha_i = 0$. The linear behavior of (2.1)-(2.2) is only valid in the linear approximation area as defined by the dashed line in Figure 2.5. To accurately model the vehicles behavior for larger slip angles a nonlinear tyre model is required and this is one of the issues the nonlinear model in section 2.2 deals with.

The bicycle model consists of two degrees of freedom, namely the side slip angle, β, and the vehicle yaw rate, $\dot{\Psi}$. The governing equations of motions can be derived from Newton's second law yielding

$$m(v_x\dot{\Psi} + \dot{v}_y) = \sum F_y = F_{y,f}\cos\delta_F + F_{y,r} \tag{2.3}$$
$$M_z = I_z\ddot{\Psi} = l_f F_{y,f}\cos\delta_F - l_r F_{y,r} \tag{2.4}$$

where m represents the vehicle mass, I_z the vehicle moment of inertia around the z-axis and l_f and l_r the distances between the vehicle CoG and the front and rear axis respectively. From Figure 2.1 the relationship $\tan\beta = \frac{v_y}{v_x}$ can be found and by assuming small angles ($\tan\beta \approx \beta$), $\dot{v}_y$ can be written as $\dot{v}_y = \frac{d}{dt}(\beta v_x) = v_x\dot{\beta} + \dot{v}_x\beta$. Inserting this relationship together with the expressions for the lateral forces (2.1) - (2.2) into (2.3) - (2.4) yields

$$m(v_x\dot{\Psi} + v_x\dot{\beta} + \dot{v}_x\beta) = C_{\alpha f}\alpha_f\cos\delta_F + C_{\alpha r}\alpha_r \tag{2.5}$$
$$I_z\ddot{\Psi} = l_f C_{\alpha f}\alpha_f\cos\delta_F - l_r C_{\alpha r}\alpha_r. \tag{2.6}$$

The slip angles can be defined in terms of the vehicle motion variables, $\dot{\Psi}$ and β. The expression for the front wheel side slip angle can be formulated by considering the velocity of the center point of the front wheel being $(v_x, v_y + l_f\dot{\Psi})$,

$$\tan(\delta_F - \alpha_f) = \frac{v_y + l_f\dot{\Psi}}{v_x} \tag{2.7}$$

and similarly for the rear wheel,

$$\tan\alpha_r = \frac{-v_y + l_r\dot{\Psi}}{v_x}. \tag{2.8}$$

Assuming small angles and again recognizing $\frac{v_y}{v_x} \approx \beta$ yields the final slip angle expressions used by the bicycle model,

$$\alpha_f = \delta_F - \beta - \frac{l_f\dot{\Psi}}{v_x} \tag{2.9}$$
$$\alpha_r = -\beta + \frac{l_r\dot{\Psi}}{v_x}. \tag{2.10}$$

Inserting these expressions into (2.5) - (2.6) together with assuming small steering angles yields the following equations of lateral and yaw motion,

$$mv_x\dot{\Psi} + mv_x\dot{\beta} + m\dot{v}_x\beta = C_{\alpha f}(\delta_F - \beta - \frac{l_f\dot{\Psi}}{v_x}) + C_{\alpha r}(-\beta + \frac{l_r\dot{\Psi}}{v_x}) \tag{2.11}$$
$$I_z\ddot{\Psi} = l_f C_{\alpha f}(\delta_F - \beta - \frac{l_f\dot{\Psi}}{v_x}) - l_r C_{\alpha r}(-\beta + \frac{l_r\dot{\Psi}}{v_x}). \tag{2.12}$$

which can be rewritten into

$$mv_x\dot{\beta} = -\beta(C_{\alpha f} + C_{\alpha r} + m\dot{v}_x) - \dot{\Psi}(mv_x + \frac{C_{\alpha f}l_f}{v_x} - \frac{C_{\alpha r}l_r}{v_x}) + \delta_F C_{\alpha f} \tag{2.13}$$

$$I_z\ddot{\Psi} = -\beta(C_{\alpha f}l_f - C_{\alpha r}l_r) - \dot{\Psi}(\frac{C_{\alpha f}l_f^2 + C_{\alpha r}l_r^2}{v_x}) + \delta_F C_{\alpha f}l_f. \tag{2.14}$$

Or, on state space form,

$$\begin{pmatrix}\dot{\beta}\\ \ddot{\Psi}\end{pmatrix} = \begin{pmatrix}\frac{-C_{\alpha f}-C_{\alpha r}-m\dot{v}_x}{mv_x} & \frac{-l_fC_{\alpha f}+l_rC_{\alpha r}}{mv_x{}^2} - 1\\ \frac{-l_fC_{\alpha f}+l_rC_{\alpha r}}{I_z} & \frac{-l_f{}^2C_{\alpha f}-l_r{}^2C_{\alpha r}}{I_zv_x}\end{pmatrix}\begin{pmatrix}\beta\\ \dot{\Psi}\end{pmatrix} + \begin{pmatrix}\frac{C_{\alpha f}}{mv_x}\\ \frac{l_fC_{\alpha f}}{I_z}\end{pmatrix}\delta_F.$$

Since not only the yaw rate is of interest here but also the lateral acceleration, the aim when constructing our sensor equation is to incorporate the lateral acceleration into the model. This can be done by utilizing the relationship $a_y = v(\dot{\beta}+\dot{\Psi}) = \frac{v_x}{\cos\beta}(\dot{\beta}+\dot{\Psi})$ [5]. By again assuming a small vehicle side slip angle, this expression becomes $a_y = v_x(\dot{\beta}+\dot{\Psi})$ where $\dot{\beta}$ can be found in (2.13). The lateral acceleration can now be represented by

$$a_y = v_x(\dot{\beta}+\dot{\Psi}) = v_x(\beta\frac{-C_{\alpha f}-C_{\alpha r}-m\dot{v}_x}{mv_x} + \dot{\Psi}(\frac{-C_{\alpha f}l_f + C_{\alpha r}l_r}{mv_x^2} - 1) + \frac{C_{\alpha f}}{mv_x}\delta_F + \dot{\Psi}) \tag{2.15}$$

which can be rewritten into

$$a_y = \beta\frac{-C_{\alpha f}-C_{\alpha r}-m\dot{v}_x}{m} + \dot{\Psi}(\frac{-C_{\alpha f}l_f + C_{\alpha r}l_r}{mv_x}) + \frac{C_{\alpha f}}{m}\delta_F. \tag{2.16}$$

On state space form the measurement equations become

$$\begin{pmatrix}a_y\\ \dot{\Psi}\end{pmatrix} = \begin{pmatrix}\frac{-C_{\alpha f}-C_{\alpha r}-m\dot{v}_x}{m} & \frac{-l_fC_{\alpha f}+l_rC_{\alpha r}}{mv_x}\\ 0 & 1\end{pmatrix}\begin{pmatrix}\beta\\ \dot{\Psi}\end{pmatrix} + \begin{pmatrix}\frac{C_{\alpha f}}{m}\\ 0\end{pmatrix}\delta_F$$

and the final state space model for the linear bicycle model with $x = [\beta, \dot{\Psi}]^T$, $y = [a_y, \dot{\Psi}]^T$ and $u = \delta_F$ results in

$$\dot{\mathbf{x}} = A\mathbf{x} + B\mathbf{u} \tag{2.17}$$

$$\mathbf{y} = C\mathbf{x} + D\mathbf{u} \tag{2.18}$$

where

$$\mathbf{A} = \begin{pmatrix}\frac{-C_{\alpha f}-C_{\alpha r}-m\dot{v}_x}{mv_x} & \frac{-l_fC_{\alpha f}+l_rC_{\alpha r}}{mv_x{}^2} - 1\\ \frac{-l_fC_{\alpha f}+l_rC_{\alpha r}}{I_z} & \frac{-l_f{}^2C_{\alpha f}-l_r{}^2C_{\alpha r}}{I_zv_x}\end{pmatrix}, \mathbf{B} = \begin{pmatrix}\frac{C_{\alpha f}}{mv_x}\\ \frac{l_fC_{\alpha f}}{I_z}\end{pmatrix}$$

$$\mathbf{C} = \begin{pmatrix}\frac{-C_{\alpha f}-C_{\alpha r}-m\dot{v}_x}{m} & \frac{-l_fC_{\alpha f}+l_rC_{\alpha r}}{mv_x}\\ 0 & 1\end{pmatrix}, \mathbf{D} = \begin{pmatrix}\frac{C_{\alpha f}}{m}\\ 0\end{pmatrix}.$$

The resulting model (2.17)-(2.18) is time-varying and linear if and only if the signals v_x and $\dot{v}_x$ are considered known.

For the online implementation the model (2.17)-(2.18) has been discretized using zero-order hold on the inputs and a sample time of 10 ms. The resulting discrete model becomes

$$\mathbf{x}[\mathbf{k}+\mathbf{1}] = A\mathbf{x}[\mathbf{k}] + B\mathbf{u}[\mathbf{k}] \tag{2.19}$$

$$\mathbf{y}[\mathbf{k}] = C\mathbf{x}[\mathbf{k}] + D\mathbf{u}[\mathbf{k}]. \tag{2.20}$$

2.1.1 Steering rack nonlinearity

In the state space model (2.17)-(2.18) the road wheel angle, δ_F, is considered an input, however no sensor is available for directly measuring this angle. Instead the AFS system supplies a sensor measuring the pinion angle, δ_G (see Figure 1.2), which has been utilized. The relationship between pinion angle and road wheel angle is however nonlinear in its nature. Figure 2.2 shows the pinion angle, δ_G, plotted against the average road wheel angle, $\delta_{F,mid}$, and as can be seen the ratio between them is not linear.

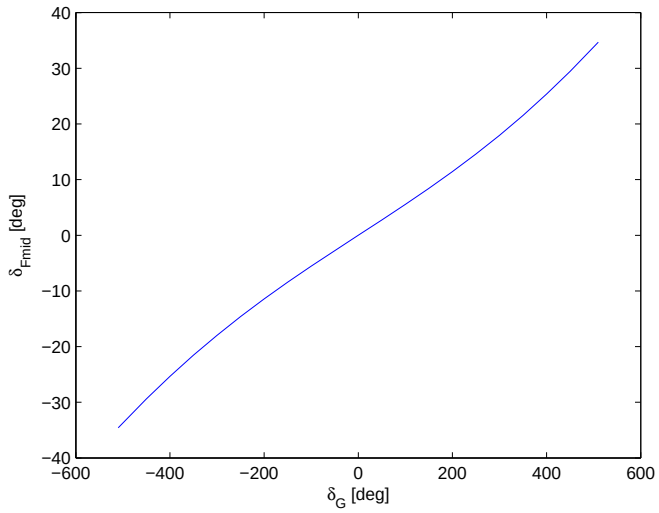

Figure 2.2: Average road wheel angle, $\delta_{F,mid}$ for the front wheels plotted against pinion angle, δ_G.

Since this information was already available for the studied vehicle the problem with the nonlinearity has been solved by using a lookup table, i.e. an approximation based on measured data.

2.1.2 Estimation of bicycle model parameters

The parameters included in the bicycle model are listed in Table 2.1. The vehicles total mass along with vehicle specific measures have been obtained by simple measurements. The location of the vehicle CoG in the plane has been calculated based on simultaneous measurements of the weight on all four tyres. These parameters have therefore been commented as *measured* in Table 2.1.

Bicycle model parameters

Parameter	Notation	Unit	Comment
Distance between rear axis and CoG	l_r	m	measured
Distance between front axis and CoG	l_f	m	measured
Vehicle mass	m	kg	measured
Yaw moment of inertia	I_z	kgm^2	estimated
Front cornering stiffness	$C_{\alpha f}$	N/rad	estimated
Rear cornering stiffness	$C_{\alpha r}$	N/rad	estimated

Table 2.1: Bicycle model parameters.

The yaw moment of inertia together with the cornering stiffnesses for both the front and rear axis have been estimated and the Matlab Optimization Toolbox and the least squares method has been used for this purpose. A residual is first created as the difference between measured yaw rate and the estimate provided from the bicycle model as seen in Figure 2.3.

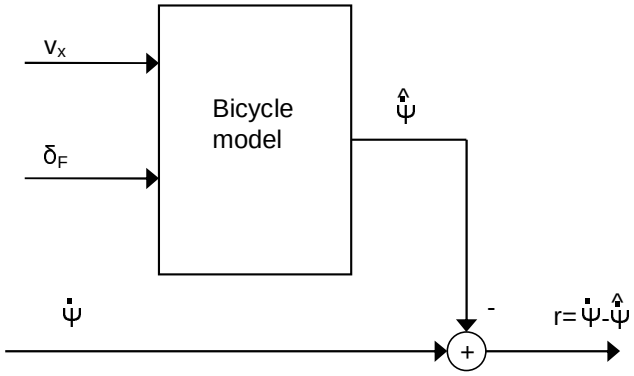

Figure 2.3: Parameter estimation procedure for the linear bicycle model.

Next, a quality function, S, is set up as the summed square of the residuals

$$S(p) = \sum_{n=1}^{N} r_n^2 = \sum_{n=1}^{N} (\dot{\Psi}_{S,n} - \hat{\dot{\Psi}}_{M,n})^2 \tag{2.21}$$

where index n represents the current sample and N the total amount of samples in the data set. The quality function depends on the parameter vector, p, that contains the parameters to optimize, i.e. $p = [I_z, C_{\alpha,f}, C_{\alpha,r}]^T$. The goal is now to minimize (2.21) with respect to this parameter vector. Figure 2.4 shows the resulting discrepancy between measured and estimated yaw rate for a handling course maneuver with optimized parameters.

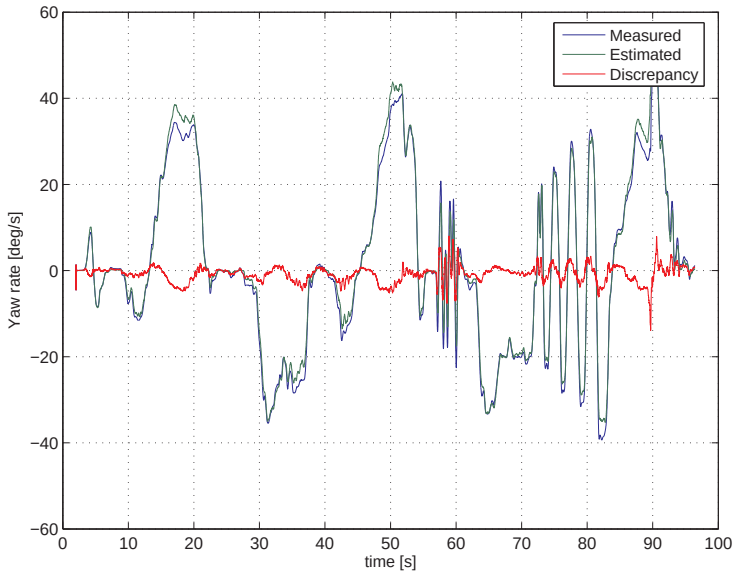

Figure 2.4: Measured vs. estimated yaw rate plotted together with the discrepancy for a handling course maneuver on asphalt. The estimate is given by the linear bicycle model with optimized parameters.

An important factor that highly influences the estimation of the cornering stiffnesses is the current surface adhesion. Figure 2.5 shows the typical relationship between slip angle and lateral force for a rear tyre. As previously mentioned, the cornering stiffness is the slope of this curve at $\alpha = 0$ and it can be seen that the slope varies between different surfaces. This surface dependency is however not addressed in this thesis, instead the current coefficient of friction is assumed to be known at all times. This requires estimation of the cornering stiffnesses on various surfaces since this parameter is surface dependent. For more information about friction estimation see [1] which is a master thesis that was performed in parallel to this thesis. Also noticeable in Figure 2.5 is that the linear relationship between lateral force and slip angle that the bicycle model uses is only

valid for slip angles up to around 4-6 degrees, or to the left of the dashed line in Figure 2.5. For larger slip angles the linear relationship will no longer provide a good approximation.

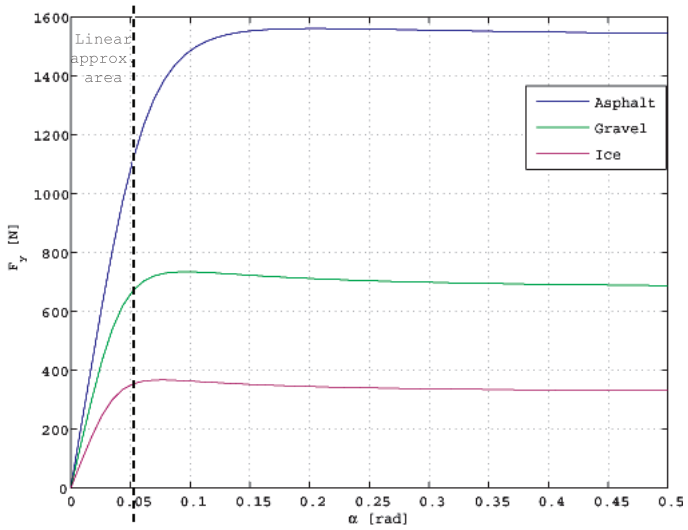

Figure 2.5: Typical nonlinear characteristic for the lateral wheel force. Here plotted against the slip angle for a rear tyre. The linear approximation area can be seen to the left of the dashed line.

2.1.3 Validity of the bicycle model

The linear bicycle model provides a good estimate of both the yaw rate and the lateral acceleration signals during steady driving maneuvers. I.e. when driving on dry and non-slippery surfaces and for moderate lateral forces. However for large slip angles when the slip angles become so large that the vehicle leaves the linear area seen in Figure 2.5 the estimates will start to deviate from the measurements. The driving maneuver seen in Figure 2.6 comes from taking sharp turns when driving straight forward at a constant speed causing high lateral acceleration peaks. This maneuver exemplifies the problems originating from large slip angles and it can be seen that the model overestimates both the yaw rate and the lateral acceleration for this maneuver. Furthermore the bicycle model lumps the two tyres on each axis together and is therefore unable to account for the effects of lateral load transfer which also will effect the model accuracy especially in sharp cornering maneuvers. In order to overcome these limitations and provide better estimates for these driving situation there is need for a more elaborate model. These are the reasons for the construction of the nonlinear two-track model that follows in the next Section.

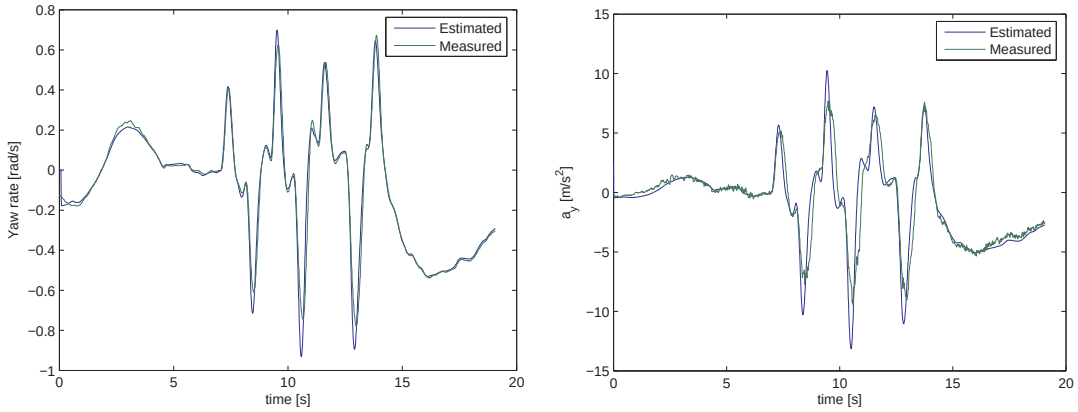

(a) Yaw rate estimate.

(b) Lateral acceleration estimate.

Figure 2.6: Bicycle model estimates for a maneuver that provokes high lateral acceleration.

2.2 Nonlinear two-track model

To include the effects of load transfer the bicycle model has been extended into a two-track model. The two-track model also incorporates a more sophisticated tyre model in order to accurately represent the tyre forces also in the nonlinear region. This section regards the derivation of this nonlinear two-track model.

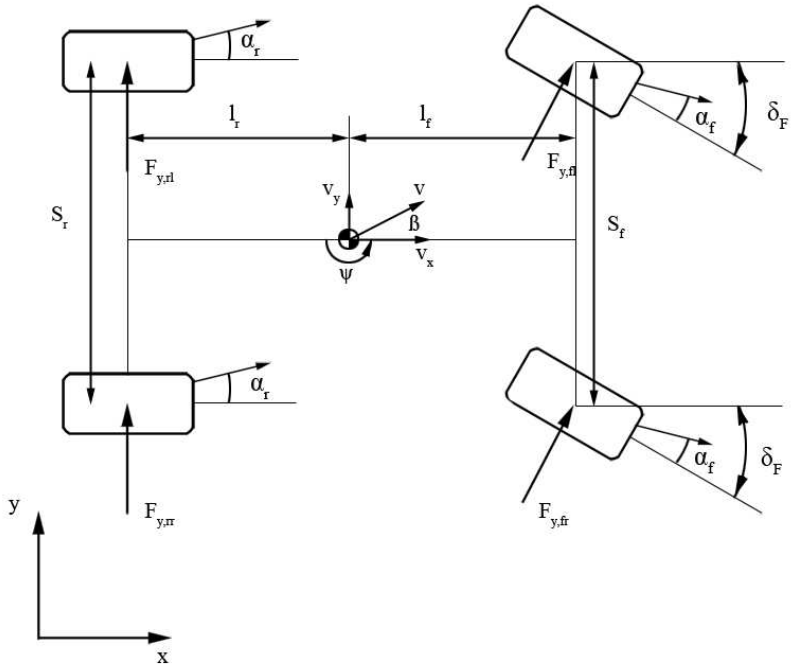

Figure 2.7: Nonlinear two-track model.

In Figure 2.7 the ingoing parameters and variables can be seen. S_r and S_f represents the rear and front track widths respectively while the rest of the parameters are the same as for the linear model seen in Figure 2.1. Just as for the linear model the longitudinal forces are neglected and Newton's second law is applied on the vehicle seen in Figure 2.7. The resulting equations of motion become

$$ma_y = F_{y,rl} + F_{y,rr} + (F_{y,fl} + F_{y,fr})\cos\delta_F \tag{2.22}$$

$$I_z\ddot{\Psi} = -l_r(F_{y,rl} + F_{y,rr}) + l_f(F_{y,fl} + F_{y,fr})\cos\delta_F - \frac{S_f}{2}((F_{y,fr} - F_{y,fl})\sin\delta_F. \tag{2.23}$$

The expression for the lateral acceleration is, just as for the linear model, $a_y = \dot{v}_y + v_x\dot{\Psi}$. v_y can be rewritten as $v_y = v_x\tan\beta$ (see Figure 2.7) and thus $\dot{v}_y = \dot{v}_x\tan\beta + v_x\frac{\dot{\beta}}{\cos^2\beta}$. By defining the road wheel angle, δ_F, as zero when facing straight forward and as increasing when the tyres are turned counter-clockwise, the resulting equations of motion for the vehicle lateral dynamics become

$$\dot{\beta} = \left(\frac{F_{y,rl} + F_{y,rr} + (F_{y,fl} + F_{y,fr})\cos\delta_F}{mv_x} - \dot{\Psi} - \frac{\dot{v}_x\tan\beta}{v_x}\right)\cos^2\beta \tag{2.24}$$

$$\ddot{\Psi} = \frac{-l_r(F_{y,rl} + F_{y,rr}) + l_f(F_{y,fr} + F_{y,fl})\cos\delta_F - \frac{S_f}{2}(F_{y,fr} - F_{y,fl})\sin\delta_F}{I_z}. \tag{2.25}$$

In order to keep the complexity of the model down, the linear relationship between slip angle and lateral force, i.e. $F_{y,ij} = C_{\alpha ij}\alpha_i$, is kept. However in order to account for load transfer effects and nonlinear tyre characteristics the cornering stiffness is now allowed to be time-varying and is also individually adapted for each tyre. The

adaptation procedure is further explained in section 2.2.1. Inserting the expression for lateral forces along with the expressions for the side slip angles (2.9)-(2.10) yields the following equations

$$\dot{\beta} = \cos^2\beta\Big\{\frac{1}{mv_x}(C_{\alpha,rl}+C_{\alpha,rr})(-\beta+\frac{l_r\dot{\Psi}}{v_x})+(C_{\alpha,fl}+C_{\alpha,fr})(\delta_F-\beta-\frac{l_f\dot{\Psi}}{v_x})\cos\delta_F- \dot{\Psi}-\frac{\dot{v}_x\tan\beta}{v_x})\Big\} \tag{2.26}$$

$$\ddot{\Psi} = \frac{1}{I_z}\Big\{-l_r(C_{\alpha,rl}+C_{\alpha,rr})(-\beta+\frac{l_r\dot{\Psi}}{v_x})+l_f(C_{\alpha,fl}+C_{\alpha,fr})(\delta_F-\beta-\frac{l_f\dot{\Psi}}{v_x})\cos\delta_F- \frac{S_f}{2}(C_{\alpha,fr}-C_{\alpha,fl})(\delta_F-\beta-\frac{l_f\dot{\Psi}}{v_x})\sin\delta_F\Big\}. \tag{2.27}$$

Finally, rearranging the equations with respect to β and $\dot{\Psi}$ yields the final nonlinear equations,

$$\dot{\beta} = \cos^2\beta\Big\{\beta(\frac{-(C_{\alpha,rl}+C_{\alpha,rr})-(C_{\alpha,fl}+C_{\alpha,fr})\cos\delta_F}{mv_x})-\frac{\dot{v}_x\tan\beta}{v_x}+ \dot{\Psi}(\frac{l_r(C_{\alpha,rl}+C_{\alpha,rr})-l_f(C_{\alpha,fl}+C_{\alpha,fr})\cos\delta_F}{mv_x^2}-1)+ \delta_F(\frac{C_{\alpha,fl}+C_{\alpha,fr}}{mv_x}\cos\delta_F)\Big\} \tag{2.28}$$

$$\ddot{\Psi} = \frac{1}{I_z}\Big\{\beta(l_r(C_{\alpha,rl}+C_{\alpha,rr})-l_f(C_{\alpha,fl}+C_{\alpha,fr})\cos\delta_F+\frac{S_f}{2}(C_{\alpha,fr}-C_{\alpha,fl})\sin\delta_F)+ \dot{\Psi}(-\frac{l_r^2}{v_x}(C_{\alpha,rl}+C_{\alpha,rr})-\frac{l_f^2}{v_x}(C_{\alpha,fl}+C_{\alpha,fr})\cos\delta_F+\frac{S_f l_f}{2v_x}(C_{\alpha,fr}-C_{\alpha,fl})\sin\delta_F)+ \delta_F(l_f(C_{\alpha,fl}+C_{\alpha,fr})\cos\delta_F-\frac{S_f}{2}(C_{\alpha,fr}-C_{\alpha,fl})\sin\delta_F)\Big\}. \tag{2.29}$$

The measurement equation can be derived by utilizing the relationship $a_y = v(\dot{\beta}+\dot{\Psi}) = \frac{v_x}{\cos\beta}(\dot{\beta}+\dot{\Psi})$ where $\dot{\beta}$ is given by (2.28).

$$a_y = \frac{v_x}{\cos\beta}(\dot{\beta}+\dot{\Psi}) = \cos\beta\Big\{\beta(\frac{-(C_{\alpha,rl}+C_{\alpha,rr})-(C_{\alpha,fl}+C_{\alpha,fr})\cos\delta_F}{m})-\dot{v}_x\tan\beta+ \dot{\Psi}(\frac{l_r(C_{\alpha,rl}+C_{\alpha,rr})-l_f(C_{\alpha,fl}+C_{\alpha,fr})\cos\delta_F}{mv_x}-v_x)+ \delta_F(\frac{C_{\alpha,fl}+C_{\alpha,fr}}{m}\cos\delta_F)\Big\}+\frac{v_x\dot{\Psi}}{\cos\beta}. \tag{2.30}$$

The final state space equations for the nonlinear two-track model with $x=[\beta,\dot{\Psi}]^T$, $y=[a_y,\dot{\Psi}]^T$ and the vector functions, $f(x,u)$ and $h(x,u)$, are described by (2.28)-(2.29) and (2.30) respectively as

$$\dot{x} = f(x,u) \tag{2.31}$$
$$y = h(x,u). \tag{2.32}$$

For the online implementation the nonlinear model has been discretized using zero-order hold on the inputs and a sample time of 10 ms. The resulting discrete model becomes

$$x_{k+1} = f(x_k,u_k) \tag{2.33}$$
$$y_k = h(x_k,u_k). \tag{2.34}$$

2.2.1 Model adaptation

The bicycle model derived in section 2.1 utilized a linear tyre model according to (2.1)-(2.2) but as mentioned in section 2.1.2 this approximation is only valid for small slip angles. Furthermore the effects of load transfer was not taken into account. In order to improve the accuracy of the two-track model even further these shortcomings need to be addressed which is done in this section by incorporating these effects into the cornering stiffnesses and thus making them time-varying variables. A block overview of the adaptation procedure can be seen in Figure 2.8. The sensor data input are the vehicle velocity, v_x, the road wheel angle, δ_F, and either the yaw rate, $\dot{\Psi}$, or the lateral acceleration, a_y. The yaw rate signal is used when estimating the lateral acceleration and vice versa. In the figure it can be seen how the vehicle side slip angle, β, that is available as a state variable from the last time step, is fed back into a block that calculates the slip angles, α for each individual tyre. These slip angles are then, together with the vertical forces, F_z, for each tyre, fed into a block that calculates the lateral forces, F_y, acting on each tyre. The block that calculates the vertical forces incorporates the effects of load transfer while the block that calculates the lateral forces incorporates the nonlinear tyre behavior. Instead of directly inserting the expressions for the lateral forces into the final nonlinear state space model (2.28)-(2.30), the expressions for the lateral forces have been divided by the slip angles to calculate new adapted cornering stiffnesses for each time instance, i.e. $C_{\alpha,ij} = \frac{F_{y,ij}}{\alpha_i}$, where index *ij* represents each of the individual tyres, fl=front left and so on. This has been done mainly in order to avoid complex mathematical expressions that would otherwise be time consuming to implement in a Simulink environment. The adaptation procedure as a whole is similar to the one used in [4].

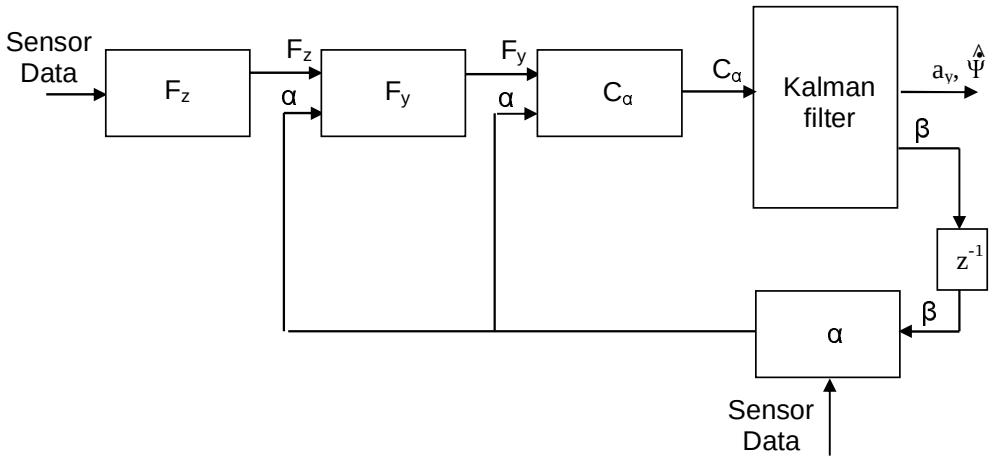

Figure 2.8: Block overview of the cornering stiffness adaptation procedure.

Vertical forces

Load transfer effects arise from cornering and vehicle roll, i.e. lateral load transfer, or similarly, braking or accelerating and vehicle pitch, i.e. longitudinal load transfer. In order to account for these effects the vertical forces for each individual wheel has to be incorporated into the model. However, as mentioned earlier the pitch motion has not been modeled in this thesis and furthermore the effects of camber angle has been neglected.
In Figure 2.9, the vertical forces, F_z, acting on each side of the vehicle along with the average track width, S_{av}, the CoG height, h_{cog}, and the forces acting at the vehicle CoG can be seen. These forces are the centripetal force, $F_{cp} = ma_y$, and the gravitational force, $F_g = mg$. By calculating the torque balances around the contact points between tyre and road, $P1$ and $P2$, the resulting vertical loads can be determined as

$$P1 : -ma_y h_{cog} + mg\frac{S_{av}}{2} - F_{z,r}S_{av} = 0 \tag{2.35}$$

$$P2 : -ma_y h_{cog} - mg\frac{S_{av}}{2} + F_{z,l}S_{av} = 0. \tag{2.36}$$

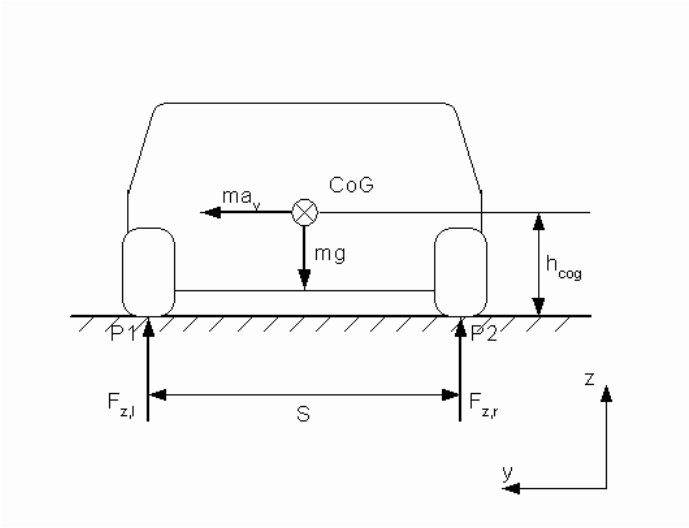

Figure 2.9: Forces acting on a vehicle seen from behind resulting in lateral load transfer. The vehicle is here driving through a right curve resulting in a lateral acceleration to the left.

Solving for the vertical forces yields the expressions used in this thesis

$$F_{z,l} = m(\frac{g}{2} + \frac{a_y m}{S_{av}}) \tag{2.37}$$

$$F_{z,r} = m(\frac{g}{2} - \frac{a_y m}{S_{av}}). \tag{2.38}$$

Here the lateral acceleration is used as an input and in order to create an estimate that is independent of the sensor signal the estimate is used here rather than the actual sensor signal.

Lateral forces

The lateral forces are now calculated by using the vertical forces along with the slip angles as input. The dependency of the vertical forces makes it possible to account for the effects of load transfer. By realizing that the relationship between lateral force and slip angle is not linear except for in a narrow region for small slip angles, see Figure 2.5, a more suitable nonlinear function should improve the model performance for larger slip angles. But first the effects of load transfer has to be incorporated and to do this each tyre has to be modeled separately. By representing the cornering stiffness on each tyre by a second (or higher) order polynomial the lateral force developed by each tyre is given by [2]

$$F_{y,ij} = C_{\alpha ij}\alpha_i = (a_{ij}F_{z,ij} - b_{ij}F_{z,ij}^2)\alpha_i = (a_{ij} - b_{ij}F_{z,ij})F_{z,ij}\alpha_i \tag{2.39}$$

where a_{ij} and b_{ij} represent the coefficients in the cornering stiffness polynomial for each tyre while $F_{z,ij}$ represent the vertical load on each tyre. In addition to this modification the nonlinear relationship between lateral force and slip angle has to be addressed. In this thesis this has been done by adapting an arctan-function to the curve seen in Figure 2.5. Other works have investigated several other elementary functions but concluded that the arctan-function provides the best fit for the lateral force curve [4]. The final expression for the lateral forces thus become

$$F_{y,ij} = (a_{ij} - b_{ij}F_{z,ij})F_{z,ij}\arctan(c_{ij}\alpha_i) \tag{2.40}$$

where α_{ij} represent the slip angles on each tyre and c_{ij} is another coefficient. The three parameters, a_{ij}, b_{ij} and c_{ij} need to be estimated for each individual tyre and the estimation procedure follows in the next section.

2.3 Estimation of two-track model parameters

When extending the model several new parameters are introduced. Vehicle specific parameters such as track width can be obtained by simple measurements. Other parameters such as those introduced to accurately model the lateral forces have to be estimated. All of the ingoing parameters in the nonlinear two-track model can be seen in Table 2.2.

Two-track model parameters

Parameter	Notation	Unit	Comment
Distance between rear axis and CoG	l_r	m	measured
Distance between front axis and CoG	l_f	m	measured
Average track width	S_{av}	m	measured
Vehicle mass	m	kg	measured
Height of CoG	h_{cog}	m	approximated
Yaw moment of inertia	I_z	kgm^2	estimated
Front cornering stiffness	$C_{\alpha,f}$	N/rad	adapted
Rear cornering stiffness	$C_{\alpha,r}$	N/rad	adapted
Lateral force coefficient	a_{ij}	-	estimated
Lateral force coefficient	b_{ij}	-	estimated
Lateral force coefficient	c_{ij}	-	estimated

Table 2.2: Two-track model parameters.

The CoG-height has been approximated as 40% of the vehicles roof height since no data or measuring method has been available for this. Remaining to be estimated are the three parameters for each wheel, a_{ij}, b_{ij} and c_{ij} from (2.40) and the yaw moment of inertia, I_z. The yaw moment of inertia is estimated in the same way as for the linear model but first the parameters a_{ij}, b_{ij} and c_{ij} are estimated and since 2.40 is nonlinear in the parameters, a nonlinear estimation method is required. The Matlab Optimization toolbox provides a nonlinear least squares solver that has been used in the estimation procedure. The Matlab code realizes the optimization algorithm and allows it to work in conjunction with the Simulink interface. I.e. the optimization algorithm minimizes the output from the Simulink model with respect to the chosen control parameters. The control parameters as well as the output are chosen by the user. Here the output is represented by the differences between the modeled and the measured lateral forces while the control parameters to be optimized are a_{ij}, b_{ij} and c_{ij}. A residual is thus created as the difference between the measured lateral force and the estimated one as

$$r_n = F_{y,n} - \hat{F}_{y,n} \tag{2.41}$$

where index n represents the current sample. Then a quality function is created as the summed square of residuals

$$S = \sum_{n=1}^{N} r_n^2 = \sum_{i=1}^{N} (F_{y,n} - \hat{F}_{y,n})^2 \tag{2.42}$$

where N is the total amount of samples in the data set. Inserting (2.40) in (2.42) yields

$$S_{ij} = \sum_{n=1}^{N} (F_{y,n} - (a_{ij} - b_{ij} F_{z,n}) F_{z,n} \arctan(c_{ij} \alpha_n))^2 \tag{2.43}$$

The optimization algorithm now minimizes (2.43) with respect to the parameters a_{ij}, b_{ij} and c_{ij}. The Levenberg-Marquardt method of optimization has been used in order to achieve guaranteed convergence in the long run. For a more detailed description of the Levenberg-Marquardt method the Matlab help section can be consulted. The measured forces have been obtained from a BMW-545i equipped with sensors measuring the tyre forces in the x- y- and z-directions as well as sensors measuring the vehicles lateral velocity. The measured lateral and vertical forces along with the slip angles calculated by means of (2.9) - (2.10) have been utilized in order to find the best parameter set that minimizes (2.42).

2.3.1 Validity of the two-track model

Figure 2.10 shows the measured versus the resulting modeled lateral force with optimized parameters for the front left tyre during a handling course maneuver. The resulting parameter values for each tyre can be seen in Appendix A.

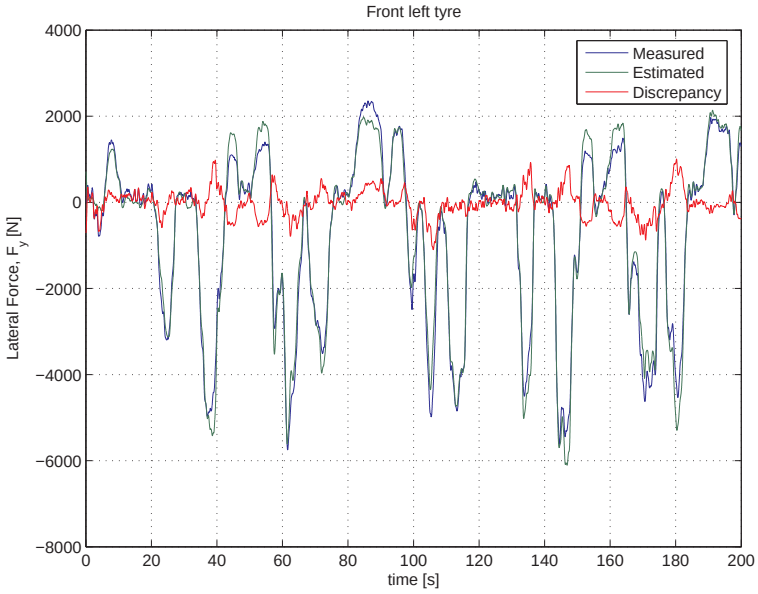

Figure 2.10: Measured vs. estimated lateral force for the front left tyre plotted together with the discrepancy for a handling course maneuver on asphalt. The estimate is given by the nonlinear two-track model with optimized parameters.

The resulting cornering stiffnesses for a circular drive at constant velocity can be seen in Figure 2.11. In the figure the cornering stiffnesses on the inner (in this case left) wheel pair are much smaller than those for the outer wheel pair. This is since the cornering stiffness can be interpreted as a measure of how well the tyre transmits forces in the lateral direction. Due to roll of the vehicle this ability will be larger for the outer wheels.

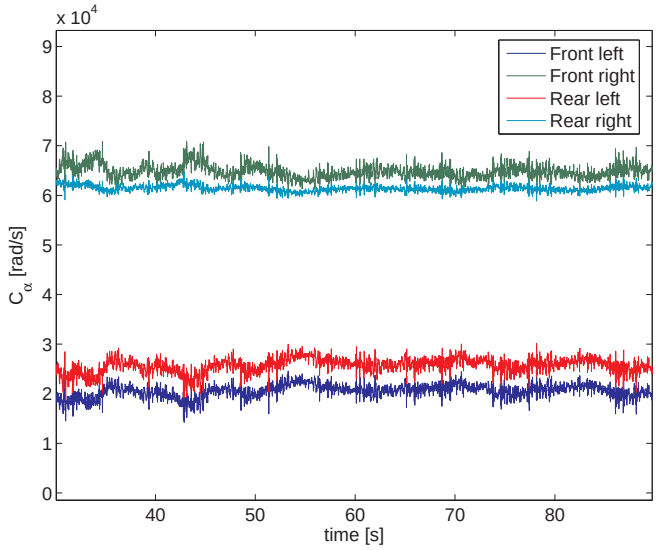

Figure 2.11: Adapted Cornering Stiffnesses on all four wheels during a counter clockwise circular drive.

Further validation of the nonlinear two-track model can be found by investigating the driving maneuver from Figure 2.6. This high lateral acceleration maneuver proved to be difficult for the bicycle model. However by studying Figure 2.12 it is clear that the nonlinear model provides a much better estimate.

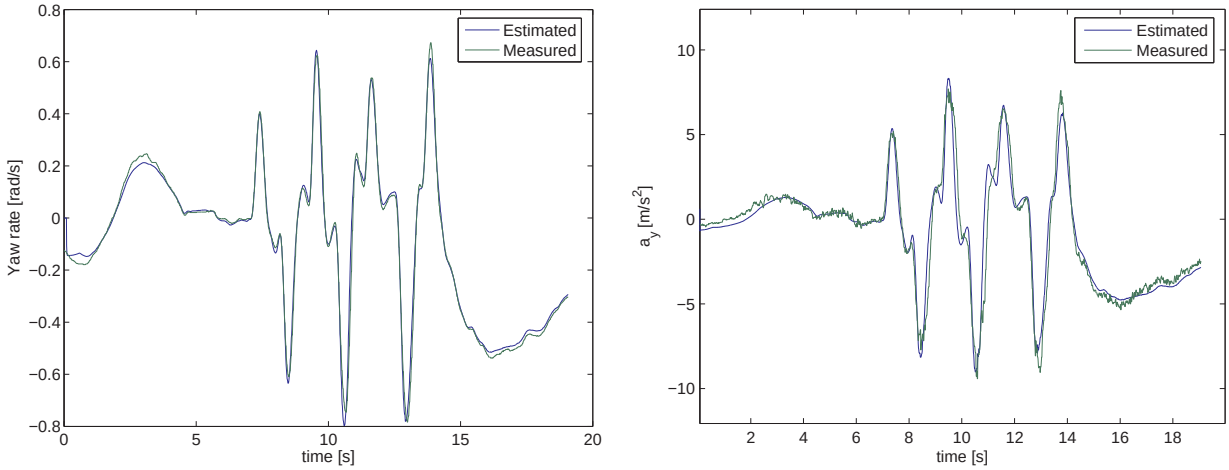

(a) Yaw rate estimate.

(b) Lateral acceleration estimate.

Figure 2.12: Nonlinear model estimates for a high lateral acceleration maneuver.

Chapter 3

Observer theory

For both the linear and the nonlinear vehicle models derived in Chapter 2, the Kalman filtering technique has been utilized when generating residuals for the sensor signals. The following chapter gives a general introduction to the underlying theory behind the Kalman filter and the Extended Kalman Filter as well as a brief overview of using observers in the context of residual generation. For a more thorough explanation of the Kalman filters than what is given here, see for instance [3] or [8]. Furthermore this chapter also deals with the derivation of the covariance matrices as well as the important issues of observability and stability.

3.1 Linear time-varying Kalman filter

The underlying idea is to use the Kalman filter as a residual generator for the linear model. This is done by feeding the input signals and the measured signals to the Kalman filter which will, under certain model assumptions, transform these into a sequence of residuals that resemble white noise. The model is thus run in parallel with the process and the residuals are calculated as the difference. Since the state matrices, A-D, include parameters that vary in time, such as the vehicle longitudinal velocity and acceleration they must be considered as time-varying and we thus need to implement the time-varying version of the Kalman filter. The process to be estimated can then be specified on the following general, time-varying, state space form

$$\begin{aligned} x_{k+1} &= A_k x_k + B_k u_k + w_k \quad & w_k \sim N(0, Q) \\ y_k &= C_k x_k + D_k u_k + v_k \quad & v_k \sim N(0, R) \end{aligned}$$

where y_k is a vector containing the measured signals, $A_k - D_k$ are known (time-varying) matrices and x_k is the state vector. The inputs are the observable u_k, the non-observable process noise, w_k, and the measurement noise, v_k. The intensities of the noises are described by the covariance matrices, Q and R. The Kalman filter is then given by

$$\hat{x}_{k+1} = A_k \hat{x}_k + B_k u_k + K_k r_k \tag{3.1}$$

$$r_k = y_k - \hat{y}_k = y_k - (C_k \hat{x}_k^- + D_k u_k). \tag{3.2}$$

Here r_k represents the vector of residuals and is created as the difference between the measured signal and the modeled one. The Kalman gain, K_k, is computed by the Kalman filter equations. The Kalman filter can be seen as a process estimator that uses feedback control, i.e. the filter estimates the states at a certain time and then receives feedback in the form of noisy measurements. The filter equations are therefore normally divided into time and measurement updates where the *time update* projects the current state estimate ahead in time while the *measurement update* adjust the projected estimate by an actual measurement at that time.

Discrete Kalman Filter

Time update equations:

$$\hat{x}_{k+1}^- = A\hat{x}_k + Bu_k$$
$$P_{k+1}^- = A_k P_k A_k^T + Q$$

Measurement update equations:

$$K_k = P_k^- C_k^T (C_k P_k^- C_k^T + R)^{-1}$$
$$\hat{x}_k = \hat{x}_k^- + K_k(y_k - (C_k\hat{x}_k^- + D_k u_k))$$
$$P_k = (I - K_k C_k)P_k^-$$

In the above equations, P_k represents the error covariance at step k and the superscript minus (as in for example $\hat{x}_k^-$) represent the *a priori* estimate, i.e. the estimate at step k given knowledge of the process before step k. When the superscript minus is left out the estimate is called *a posteriori* and also includes the knowledge of the measurement at that time. To sum up, the Kalman filter first projects the state estimate and the covariance estimate forward one step in time during the *time update*. Then the Kalman gain is calculated, the process is measured and an *a posteriori* state estimate is obtained. Finally the *a posteriori* error covariance matrix, P_k, is calculated.

3.2 Extended Kalman filter

Since the two-track model derived in section 2.2 is nonlinear, the Kalman filter theory from the last section can not be applied. Instead an extension of the ordinary Kalman filter that covers nonlinear problems as well has been used. The idea behind the EKF theory consist in linearizing the model around the previous state estimate in every time step. The EKF is based on (2.28)-(2.30). The observed nonlinear system can be described by

$$x_{k+1} = f(x_k, u_k) + w_k \quad w_k \sim N(0, Q) \tag{3.3}$$
$$y_k = h(x_k, u_k) + v_k \quad v_k \sim N(0, R) \tag{3.4}$$

where $f(x_k, u_k)$ represents the state equation and $h(x_k, u_k)$ the measurement equation. As earlier, w_k and v_k represent the process noise and measurement noise respectively. The Extended Kalman filter is now given by

$$\hat{x}_{k+1} = f(\hat{x}_k, u_k) + K_k r_k \tag{3.5}$$
$$r_k = y_k - \hat{y}_k = y_k - h(\hat{x}_k^-, u_k). \tag{3.6}$$

The EKF time and measurement update equations are now constructed in the same manner as for the linear Kalman filter.

Extended Kalman Filter

Time update equations:

$$\hat{x}_{k+1}^- = f(\hat{x}_k, u_k)$$
$$P_{k+1}^- = F_k P_k F_k^T + Q_k$$

Measurement update equations:

$$K_k = P_k^- H_k^T (H_k P_k^- H_k^T + R_k)^{-1}$$
$$\hat{x}_k = \hat{x}_k^- + K_k(y_k - h(\hat{x}_k^-, u_k))$$
$$P_k = (I - K_k H_k)P_k^-$$

F_k and H_k represent the linearized versions of the matrices A_k and C_k. The best linear approximation to a difference function near a given point is given by the Jacobian matrix. The Jacobian matrix consists of a certain (vector-valued) function's all first order partial derivatives. The Jacobian matrices corresponding to matrices $A_k - D_k$ are defined as

$$F_{i,j} = \frac{\partial f_i}{\partial x_j}(\hat{x}_{k-1}, u_{k-1}) \tag{3.7}$$

$$B_{i,j} = \frac{\partial f_i}{\partial u_j}(\hat{x}_{k-1}, u_{k-1}) \tag{3.8}$$

$$H_{i,j} = \frac{\partial h_i}{\partial x_j}(\hat{x}_{k-1}, u_{k-1}) \tag{3.9}$$

$$D_{i,j} = \frac{\partial h_i}{\partial u_j}(\hat{x}_{k-1}, u_{k-1}) \tag{3.10}$$

The Jacobian matrices for the nonlinear two-track model with their ingoing partial derivatives can be found in Appendix B.

3.3 Determining Covariance matrices

In order to reduce the complexity of the problem, both the measurement covariance matrix and the process covariance matrix are assumed diagonal. That means that both the measurement noise and the process noise are assumed to be uncorrelated.

The measurement covariance matrix, R, is used to define the error on the sensor measurement. The sensor noise levels are known from the sensor manufacturers data sheets and the measurement covariance matrix is therefore comprised of the square of the corresponding sensor noise levels. The measurement noise does however also depend on surface since non-smooth surfaces add to the sensor vibrations. Especially the lateral acceleration sensor shows large measurement noise when driving on low-μ surfaces. An approximation can be achieved by high pass filtering the the lateral acceleration signal and assuming that the remaining signal is comprised of sensor noise. Figure 3.1 shows a histogram of the high pass filtered lateral acceleration signal for a handling course drive on ice. It can be seen that the distribution seems to approximate a normal distribution, something that further motivates the use of a Kalman filter.

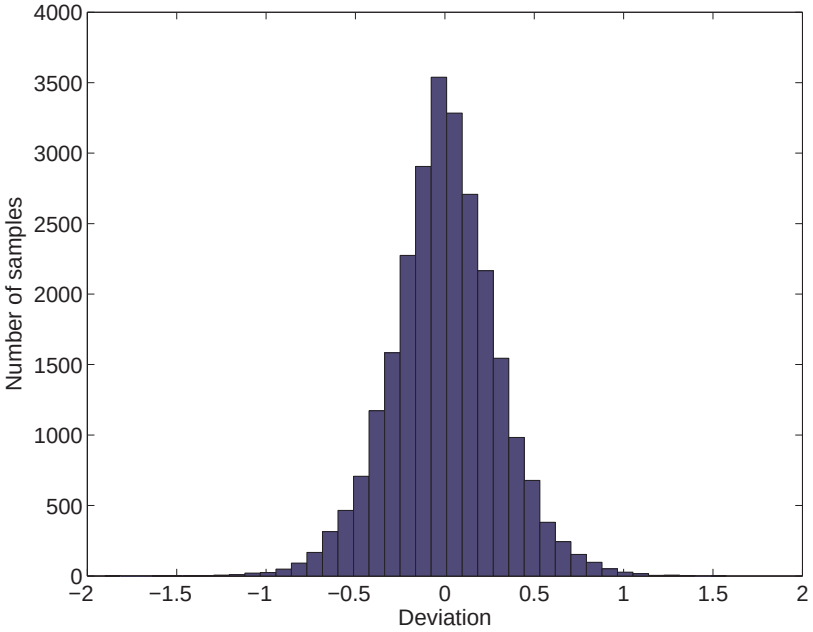

Figure 3.1: The distribution of the measurement noise on the lateral acceleration sensor.

The process noise is mainly caused by model inaccuracies and uncertainties in parameter estimates. An estimate for the process noise is achieved in a similar way as for the measurement noise. By assuming that the process noise is of low frequency character it can introduced as

$$w = f(\hat{x}, u) - \dot{\hat{x}} \tag{3.11}$$

where $\dot{\hat{x}}$ is the low pass filtered and differentiated measured state and $f(\hat{x}, u)$ is the differentiated estimated state. The calculations of R and Q can now be performed in Matlab.

Chapter 4

Kinematic relations

Apart from the residuals generated from the two Kalman filters a number of residuals have also been created based on kinematic relations. This chapter describes the origin of these residuals and also addresses the issues accompanying each relation.

Models 1-2

One way to reconstruct the yaw rate sensor is by using the wheel speed signals. This approach assumes rolling tyres and neglects the body roll angle. By studying the wheel speeds on each of the four wheels, the following relations can be set up

$$v_{fl} = (v_x - \dot{\Psi}\frac{S_f}{2})\cos\delta_F + (v_y + \dot{\Psi}l_f)\sin\delta_F \quad (4.1)$$

$$v_{fr} = (v_x + \dot{\Psi}\frac{S_f}{2})\cos\delta_F + (v_y + \dot{\Psi}l_f)\sin\delta_F \quad (4.2)$$

$$v_{rl} = v_x - \dot{\Psi}\frac{S_r}{2} \quad (4.3)$$

$$v_{rr} = v_x + \dot{\Psi}\frac{S_r}{2} \quad (4.4)$$

where S_f and S_r represent the front and rear track width respectively. Calculating the difference in wheel speed between the two tyres on each axis yields

$$v_{fr} - v_{fl} = \dot{\Psi}S_f\cos\delta_F \quad (4.5)$$

$$v_{rr} - v_{rl} = \dot{\Psi}S_r \quad (4.6)$$

or, for the yaw rate

$$\dot{\Psi}_{M1} = \frac{v_{fr} - v_{fl}}{S_f\cos\delta_F} \quad (4.7)$$

$$\dot{\Psi}_{M2} = \frac{v_{rr} - v_{rl}}{S_r}. \quad (4.8)$$

Since the tyres don't always roll but sometimes spin or lock, the assumption of rolling tyres is not always fulfilled. Especially, since the vehicle studied in this thesis is rear wheel driven, the residual that is based on the rear wheel speed signals will suffer from this and therefore the residual corresponding to the front wheels should be the more accurate of the two. This can be confirmed in Figure 4.1 where the yaw rate estimate from the first two kinematic models are compared to the sensor signal. The model based on the rear wheel speed signals deviates strongly from the measured value after around 52 seconds and between 90 and 94 seconds. In this case the inaccuracy comes from the fact that the rear left tyre spins slightly during these time instants.

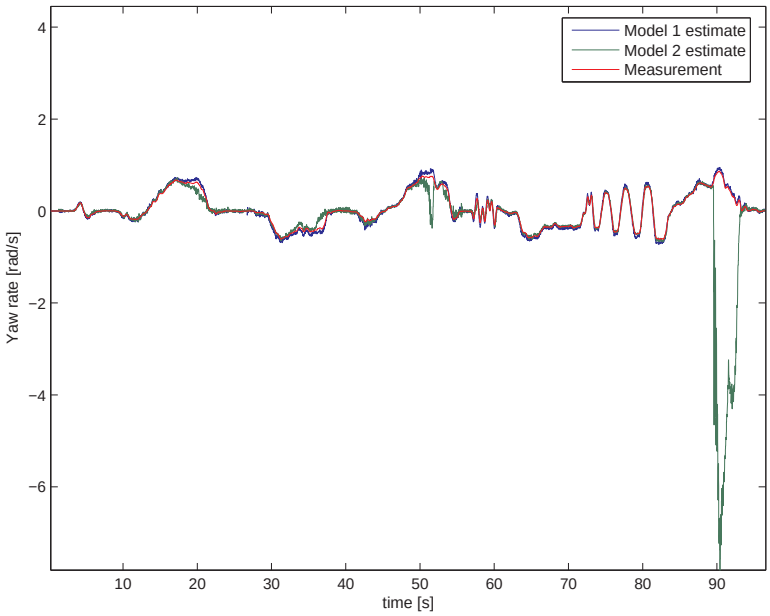

Figure 4.1: Yaw rate estimates from kinematic models using the wheel speed sensors plotted together with the measured yaw rate.

Model 3

Another estimate of the yaw rate can be derived from the vehicle longitudinal velocity, v_x and the road wheel angle, δ_F, by assuming zero side slip on all four tyres. The slip equations (2.7)-(2.8) with $\alpha_f = \alpha_r = 0$ thus become

$$\tan \delta_F = \beta + \frac{l_f \dot{\Psi}}{v_x} \tag{4.9}$$

$$0 = -\beta + \frac{l_r \dot{\Psi}}{v_x}. \tag{4.10}$$

Combining the two slip angle equations yields

$$\delta_F = \arctan\left(\beta + \frac{l_f \dot{\Psi}}{v_x}\right) = \arctan\left(\frac{l_r \dot{\Psi}}{v_x} + \frac{l_f \dot{\Psi}}{v_x}\right) = \arctan\left(\frac{l \dot{\Psi}}{v_x}\right) \tag{4.11}$$

or, for the yaw rate,

$$\dot{\Psi}_{M3} = v_x \frac{\tan \delta_F}{l}. \tag{4.12}$$

By assuming zero slip angles this model will lose accuracy in situations where the slip angles are non-neglectable. Figure 4.2 shows the yaw rate estimate against the measured yaw rate. As can be seen in the figure the amplitude is slightly larger for the estimate and it also slightly delayed. The error in amplitude comes from inherited nonlinearities in tyres, steering, power train and suspension and by slightly reducing the road wheel angle, this can be compensated for. Experiments show that a reduction of around 5% yields the best agreement for this model. Furthermore, it can also be seen that the measured yaw rate seems slightly delayed in comparison to the estimate. This is a result of differences in the filtering techniques used for the various signals and has been compensated for by delaying the measured signal with 0.1 seconds, a number also obtained through experiments. The modified residual becomes

$$\dot{\Psi}_{M3} = v_x \frac{\tan 0.95\delta_{F,d}}{l} \tag{4.13}$$

where $\delta_{F,d}$ is the delayed road wheel angle. The result can be seen in Figure 4.3.

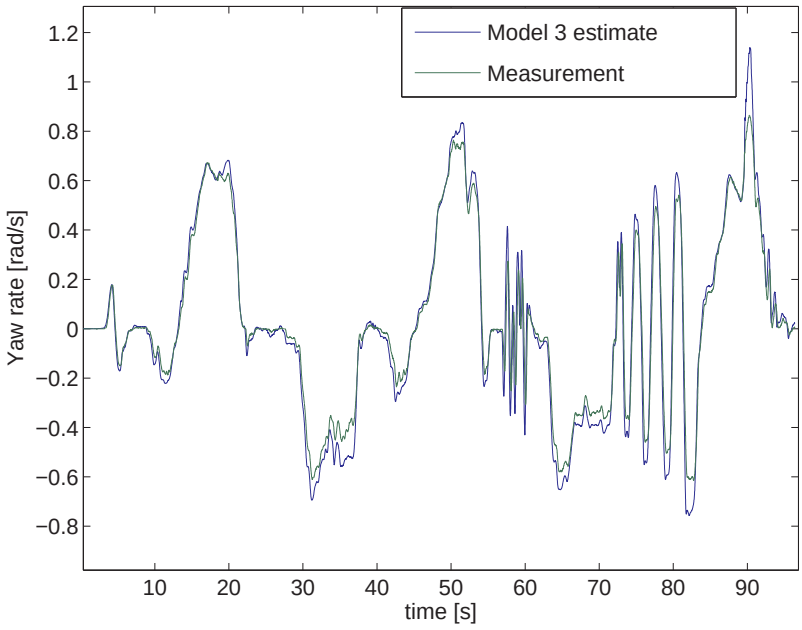

Figure 4.2: Yaw rate estimate from the kinematic relation using the pinion angle sensor plotted together with the measured yaw rate.

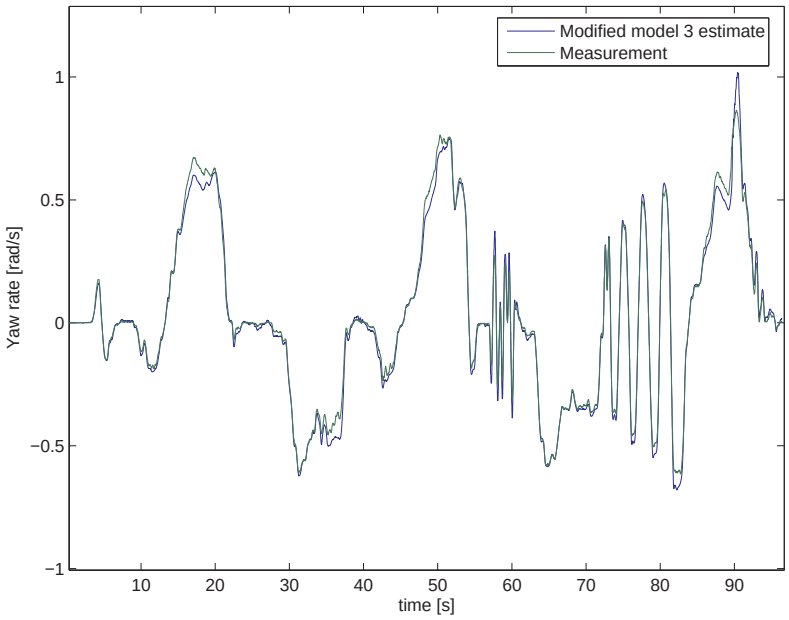

Figure 4.3: Yaw rate estimate from the modified kinematic relation using the pinion angle sensor plotted together with the measured yaw rate.

Model 4

Finally a relationship between yaw rate and lateral acceleration is set up by assuming steady state driving conditions and thus neglecting the vehicle side slip angle as

$$\dot{\Psi}_{M4} = \frac{a_y}{v_x}. \tag{4.14}$$

Figure 4.4 shows the yaw rate estimate based on the lateral acceleration sensor. One problem with this model is that the estimate becomes very noisy since it is based on the noisy lateral acceleration sensor signal. This can be

addressed by filtering the signal but this introduces an unwanted time delay.

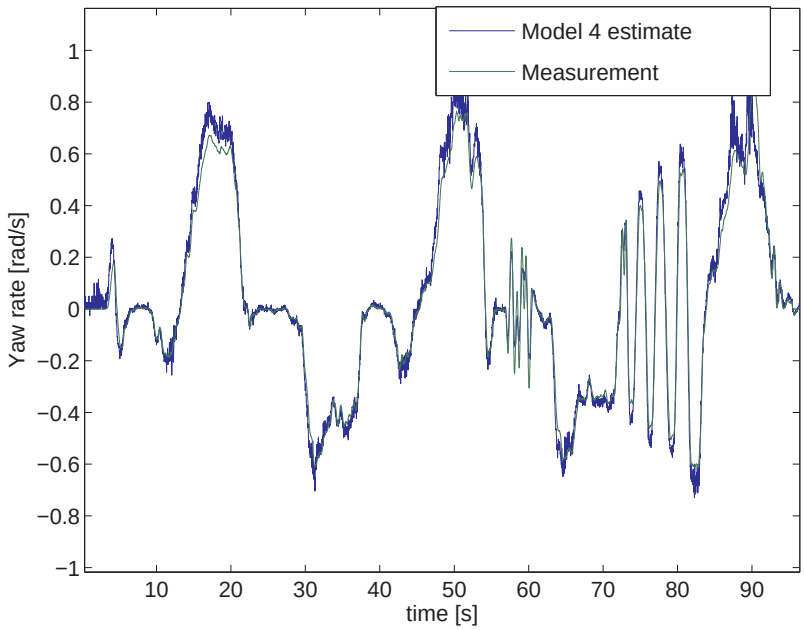

Figure 4.4: Yaw rate estimate from the kinematic relation using the lateral acceleration sensor plotted together with the measured yaw rate.

The above estimates are all for the yaw rate sensor but they can easily be adjusted to monitor the lateral acceleration by utilizing (4.14), i.e. $a_y = \dot{\Psi}_{M3} v_x$. All the kinematic relations are summarized in Table 4.1.

Kinematic relations		
	Yaw rate $[rad/s]$	Lateral acceleration $[m/s^2]$
Model 1	$\dot{\Psi}_{M1} = \frac{v_{fr} - v_{fl}}{S_f \cos \delta_F}$	$a_{y,M1} = \frac{v_{fr} - v_{fl}}{S_f \cos \delta_F} v_x$
Model 2	$\dot{\Psi}_{M2} = \frac{v_{rr} - v_{rl}}{S_r}$	$a_{y,M2} = \frac{v_{rr} - v_{rl}}{S_r} v_x$
Model 3	$\dot{\Psi}_{M3} = v_x \frac{\tan 0.95\delta_{F,d}}{l}$	$a_{y,M3} = v_x^2 \frac{\tan 0.95\delta_{F,d}}{l}$
Model 4	$\dot{\Psi}_{M4} = \frac{a_y}{v_x}$	$a_{y,M4} = \dot{\Psi} v_x$

Table 4.1: Summary of kinematic relations used.

Chapter 5

Change detection

Ideally the residuals created in the earlier chapters (or any residual for that matter) would equal zero in the fault free case and only deviate from this value when a fault occurs. However in reality neither effects from disturbances such as noise nor uncertainties in modeling or parameter estimates can be neglected. Even the most rigorous attempts to model the dynamic behavior of complex processes such as ”car driving” will suffer from modeling shortcomings in one way or another.

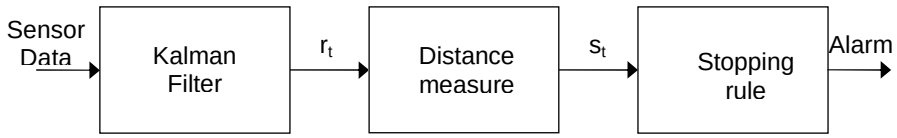

Figure 5.1: Change detection based on the kalman filter.

A block structure of a diagnosis system can be seen in Figure 5.1. The first block contains the observer that based on various sensor signals provides the residual, r_t, which here is the difference between the measured and the modeled values. This residual is then fed into a distance measure block. This block transforms the residual to a distance measure that measures the deviation from the no-change assumption. The distance measure, s_t, is then fed into a stopping rule block and that applies a decision function on the distance measure yielding a test statistic, g_t, as $g_t = g(s_t)$. This test statistic is then compared to a threshold in order to determine whether or not to raise an alarm.

5.1 Distance measures

As mentioned the distance measure transforms the residual to a distance measure that measures the deviation from the no-change assumption. There are several different types of faults that might occur and depending on which type we want to be able to detect there are different distance measures that can be applied. Sudden faults are faults that abruptly occurs and then stays that way. Drifting faults is another type of fault that gradually increases in time and there are also variance faults which effect the signal variance. A common approach when looking for sudden or drifting faults is to use the residual itself as distance measure. Another common approach is to use the squared residual which is advantageous especially when trying to detect variance faults.

5.2 Stopping rules

The change detection problem can be reformulated by using two hypothesis as

$$\begin{aligned} H_0 &: E(s_t) = 0 \\ H_1 &: E(s_t) > 0. \end{aligned}$$

A stopping rule is basically a low pass filter that is applied onto the distance measure and the result is then compared to a threshold in order to detect whether or not a fault has occurred. Examples of stopping rules often used are the Cumulative Sum (CuSum) and Geometric Moving Average (GMA) tests. The CuSum test is investigated further in section 5.2.4.

5.2.1 Direct thresholding

The simplest way to implement a stopping rule is to apply a direct threshold on the distance measure. By doing this an alarm can be raised when the distance measure exceeds the threshold, J.

$$\text{Alarm if } s_t \geq J \tag{5.1}$$

The threshold is normally chosen in advance based on noise levels, disturbances and modeling uncertainties. Since the aim of this thesis is to detect sensor faults the focus lies on fast detection while at the same time keeping the false alarm rate small. To set accurate threshold levels in an application such as this vast amounts of test data from different driving situations have to be gathered and investigated. Here the thresholds have been chosen so that no false alarms were detected for any of the data sets available during the writing of this thesis. To increase the robustness of the diagnosis system a common approach is to keep track of how many times the test statistic exceeds the threshold during a fixed time interval and not alarm until the threshold has been exceeded for a certain number of samples.

5.2.2 Adaptive thresholding

One of the problems with the direct thresholding approach is that model uncertainties force the threshold level to be set high, which in turn increases the detection times. Instead of trying to optimize the vehicle model and thus reduce model uncertainties overall, more advanced thresholding methods such as adaptive thresholding can be used. The basic idea with adaptive thresholding is to utilize information about how model uncertainties and disturbances vary in time and let the threshold vary accordingly. A general description of how the adaptive threshold, J_{adp} is computed is given by [7] as

$$J_{adp} = c_1 W(u, y) + c_2 \tag{5.2}$$

where W(u,y) is a measure of the model uncertainty while c_1 and c_2 are constants. The difficulty with using an adaptive threshold lies in finding a good model uncertainty measure.

This thesis concentrates on distinguishing between two different driving modes, steady driving and unsteady driving. When the vehicle is in the unsteady driving mode model uncertainties are effecting the residuals and the thresholds are therefore raised in order to avoid false alarms. Figure 5.2 shows how the adaptive thresholds are calculated. The first block compares the velocity, v_x, the wheel speeds, ω_i for $i \in \{1..4\}$ and the kinematic relations derived in Chapter 4 (except those that include the observed signals) to a set of critical values and can in that way determine what driving mode the vehicle is in. The set threshold block then determines the threshold depending on the current driving mode.

The vehicle is considered being in the steady driving mode when $|\dot{\Psi}_{M1}|\&|\dot{\Psi}_{M2}|\&|\dot{\Psi}_{M3}| < \dot{\Psi}_c$, $|v_x| < v_{x,c}$ and $|\dot{\delta}_G| < \dot{\delta}_{G,c}$ where index c represents critical levels. That is, when the yaw rate estimates from the kinematic relations are close to the measured yaw rate and neither the vehicle velocity nor the pinion angle velocity are too great, the vehicle is in steady driving. The critical levels have been determined by investigating the test drives performed.

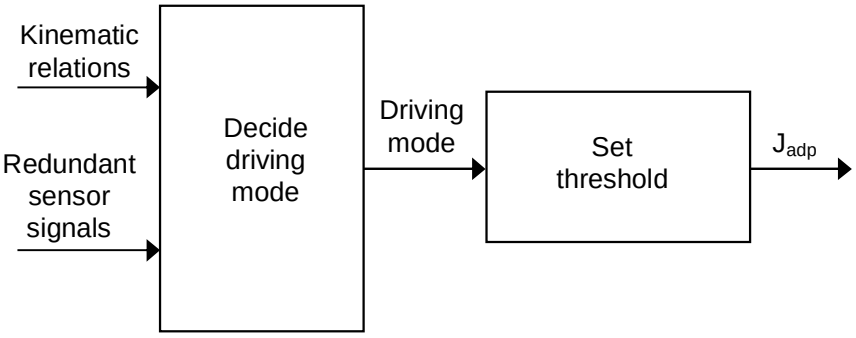

Figure 5.2: Block overview of the generation of adaptive thresholds.

Similarly the vehicle is considered being in the unsteady driving mode when either of the critical levels are exceeded. That is when $|\dot{\Psi}_{M1}| \mid |\dot{\Psi}_{M2}| \mid |\dot{\Psi}_{M3}| > \dot{\Psi}_c$ or $|v_x| > v_{x,c}$ or $|\dot{\delta}_G| > \dot{\delta}_{G,c}$.

5.2.3 Residual Filtering

One approach for handling modeling errors is to high pass filter the test statistic and then apply a direct thresholding technique in order to detect faults. The idea behind residual filtering is to choose a cutoff frequency such that it distinguishes between the driver input via the steering wheel and the occurrence of sudden faults.

The input in vehicle dynamics applications is the driver command and it generally don't exceed the frequency range of 2 Hertz and by high pass filtering the residuals using a high pass filter with a crossover frequency of 2 Hertz model uncertainties can be easier distinguished. This will however result in that if the driver is steering with a frequency larger than 2 Hertz, when trying to avoid a collision for example, this could be mistaken for a sensor fault unless it is dealt with. In order to avoid this the algorithm observes the pinion angle and the pinion angle derivative and disables the algorithm if these become too great. There are some drawbacks with this method as well. The most obvious one being that after a sensor fault occurs the residuals will only shortly deviate from their prescribed value and then return even if the fault remains. Furthermore this method is only applicable for detecting sudden faults. Drifting faults that slowly increase in time will not be detected.

5.2.4 CuSum

For more information about the nature of log-likelihood ratios and a deeper understanding of the algorithm than is presented here, see for example [3]. CuSum is short for Cumulative Sum and is a common technique used in change detection applications. The algorithm calculates the cumulative sum of variances by using the sign change that is inherited in the log-likelihood ratio

$$s_i = \ln \frac{p_{\theta_1}(y_i)}{p_{\theta_2}(y_i)}. \tag{5.3}$$

In (5.3) θ_1 and θ_2 represent two hypothesis with the probabilities $p_{\theta_1}(y_i)$ and $p_{\theta_2}(y_i)$ respectively. The probability $p_{\theta_1}(y_i)$ corresponds to the statistical distribution before a change and $p_{\theta_1}(y_i)$ corresponds to that after a change. When a change presents itself in the parameter θ, this reflects on the log-likelihood ratio (5.3) as a sign change. This property is used by the CuSum algorithm in the detection. The log-likelihood ratios are summed up as

$$S_n = \sum_{i=0}^{n} s_i \tag{5.4}$$

where s_i represents the distance measure. Given a gaussian signal with a change injected as in Figure 5.3(a), S_n will show a negative drift before the change and positive after as seen in Figure 5.3(b). A test statistic, g_t, is then created by summing up the distance measure recursively as

$$g_t = g_{t-1} + s_t \tag{5.5}$$

$$g_0 = 0. \tag{5.6}$$

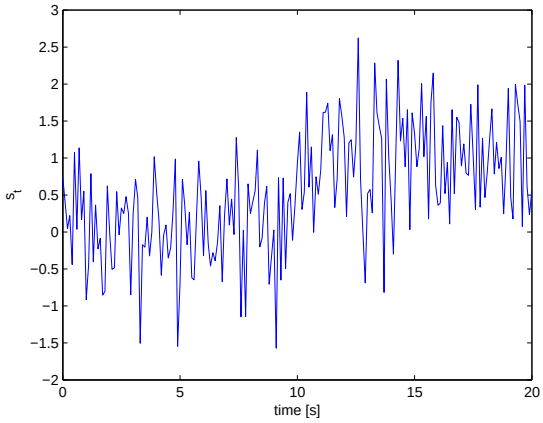

(a) A signal observed with noise.

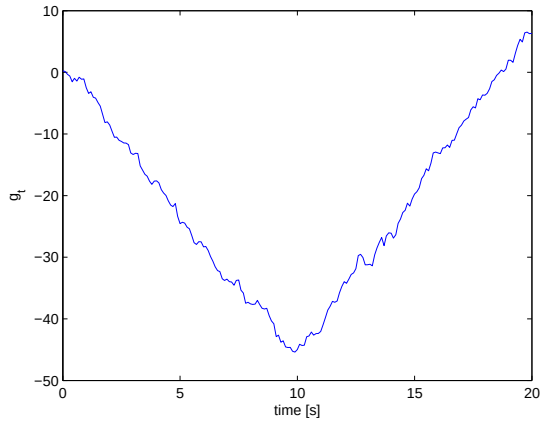

(b) The negative and positive drift of the log-likelihood ratio, S_n.

Figure 5.3: A Gaussian sequence with a bias fault injected after 10 seconds.

The CuSum algorithm now compares the current value of the test statistic with the minimum value and if this difference is larger than a preset threshold an alarm is signaled. For the sake of convenience, the test statistic is normally reset to zero every time it is drifting negatively, otherwise it would drift negatively forever in the fault-free case. Furthermore a drift parameter, ν, is introduced in order to avoid an unwanted positive drift that might occur when S_k is positive for several time instants in a row. The drift parameter is a design parameter chosen by the user. The final CuSum algorithm is represented by

$$g_t = max(g_{t-1} + s_t - \upsilon, 0) \tag{5.7}$$

$$g_0 = 0 \tag{5.8}$$

$$\text{If } g_t > h \quad : \quad g_t = 0 \text{ and alarm.} \tag{5.9}$$

Figure 5.4 shows a typical behavior for the CuSum algorithm. In the figure it can be seen how the test statistic is affected after the fault is injected. The test statistic is reset to zero every time it reaches above the threshold that in this case is set to 5. It should also be noted that this is based on a perfectly Gaussian signal.

The design parameters available for the user are the threshold, h, and the drift parameter, ν. The input to the CuSum algorithm controls the choice of these parameters and the larger the variance is the larger ν should be chosen. A good rule of thumb when choosing design parameters is to start with a very large threshold h and then choose the drift parameter ν so that g_t=0 more than 50% of the time [3]. Now set the threshold so that the required number of false alarms is obtained. The design parameters can then be tuned in order to achieve the

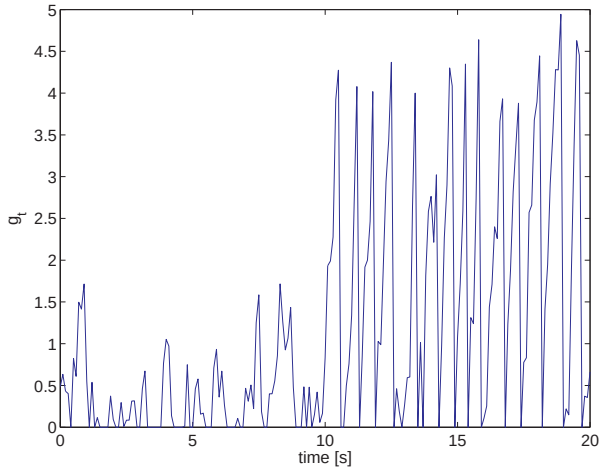

Figure 5.4: The CuSum test statistic behavior for the signal seen in Figure 5.3(a). The threshold is set at 5 and the drift parameter is set to 0.25.

desired performance. Also note that a change smaller than ν will not be detectable. The threshold depends on both the input signal and the drift parameter. If ν is chosen big, the random positive will be small making it possible to choose h small in order to achive faster fault detection. In this thesis the parameters have been chosen based on these rules of thumb.

Chapter 6

Results

In this chapter some results achieved from using the various kinematic relations from Chapter 4 together with the change detection methods described in Chapter 5 are presented. Apart from the results achieved from using the kinematic relations all of the residuals shown in this chapter are based on the nonlinear two-track model derived in section 2.2. The plotted residuals are created as the difference between measured and estimated signal, i.e. $r = \hat{y}_i - y_i$ where index i represents the two different sensors that are to be plausibilisated and when the occurrence of faults have been simulated it has been done in a Simulink environment. The figures presented in this chapter are often displayed two and two and when this is the case the left figure represent the yaw rate while the right one represents the lateral acceleration. Furthermore, all figures in this chapter are results of simulations based on test data sequences acquired from various test drives made with the prototype vehicle at hand, namely a BMW-545i.

6.1 Kinematic relations

The different kinematic relations derived in Chapter 4 are here investigated and compared against each other. The second kinematic model (4.8) has been left out since it is similar to the first model (4.7) but not as accurate since the vehicle investigated was rear wheel driven.

Figures 6.1(a)-6.1(b) represent the yaw rate and lateral acceleration estimates for the three kinematic models when performing an ISO (International Organization for Standardization) lane change maneuver on asphalt. Figures 6.1(c)-6.1(d) show the respective residuals and it can be noted that the residuals are quite small and it is concluded that the kinematic relations work well in these, rather kind, circumstances. Especially the model based on the steering wheel angle (4.13) provides a good estimate for both the yaw rate and the lateral acceleration for this maneuver.

A handling course maneuver performed on ice has also been evaluated and the results are shown in Figure 6.2. The first observation that can be made is how noisy all the signals are. This is because vibrations increase the measurement noise on ice. In Figures 6.2(c)-6.2(d) the same estimates are plotted but here the sensor signals have been low pass filtered using a butterworth filter of grade 2 and thus filtering away a lot of the noise. Figures 6.2(e)-6.2(f) show the residuals and very large peaks can be seen in mainly the model 1 and model 4 residuals. These come from large variations in the sensor signals coming from the wheel speed sensors and the vehicle velocity respectively.

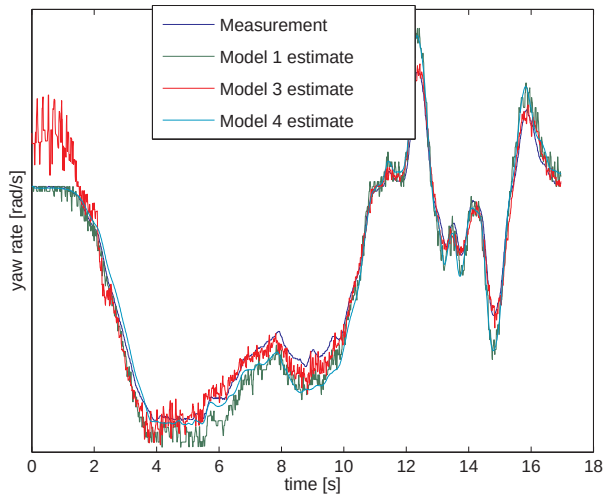

(a) Measured vs. estimated yaw rate.

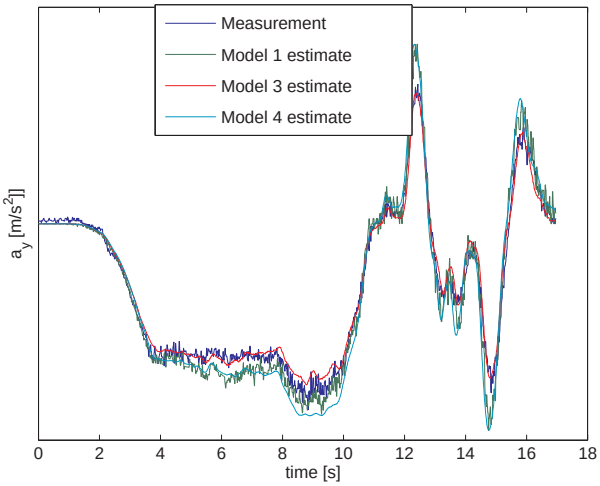

(b) Measured vs. estimated lateral acceleration.

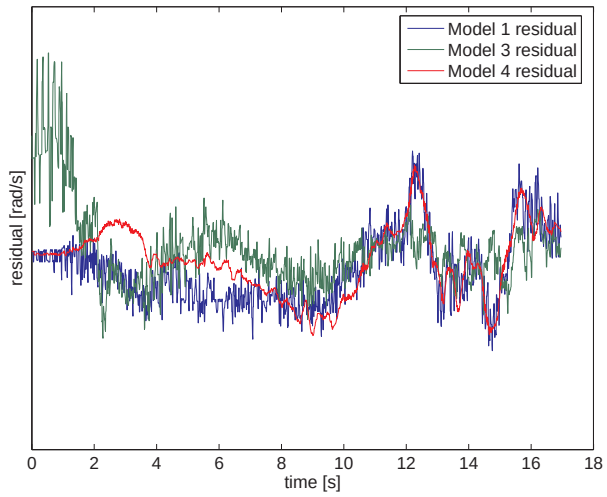

(c) Yaw rate residual.

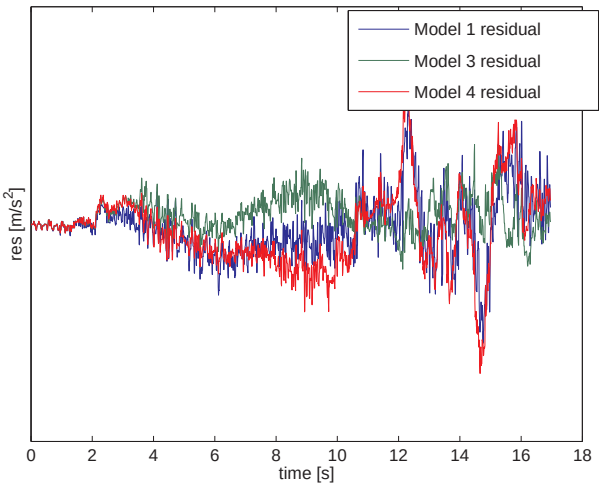

(d) Lateral acceleration residual.

Figure 6.1: Yaw rate and lateral acceleration estimates based on the kinematic models for an ISO lane change maneuver performed on asphalt.

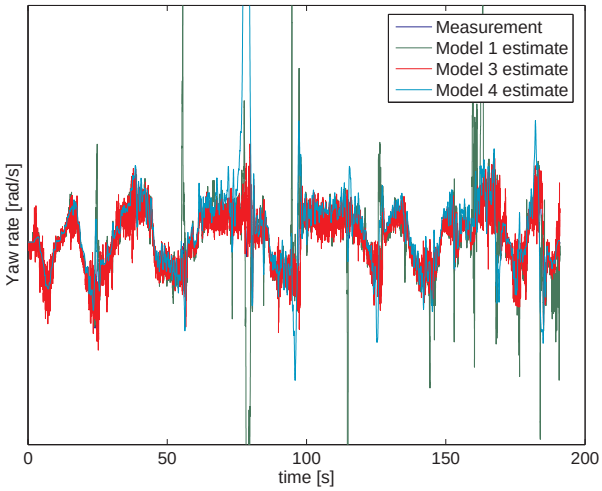

(a) Measured vs. estimated yaw rate.

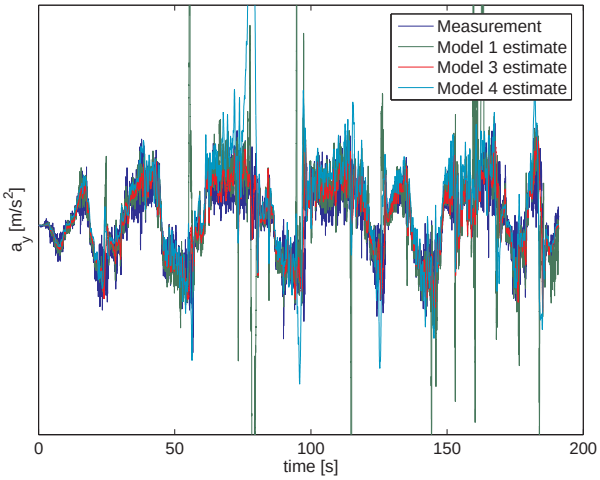

(b) Measured vs. estimated lateral acceleration.

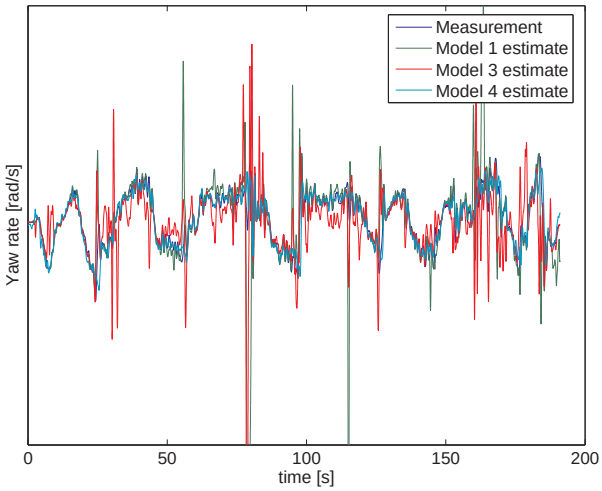

(c) Measured vs. estimated yaw rate (filtered).

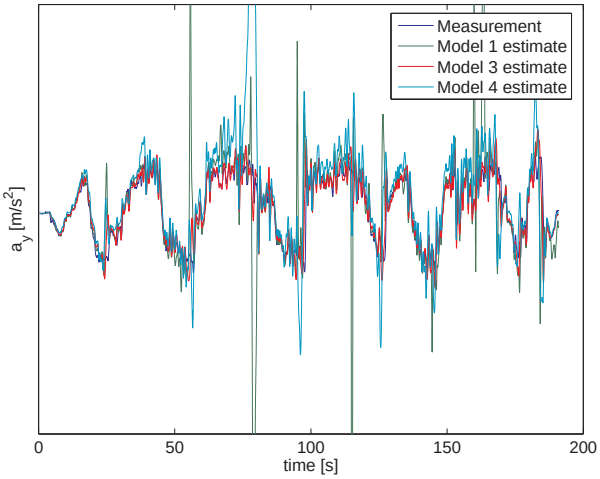

(d) Measured vs. estimated lateral acceleration (filtered).

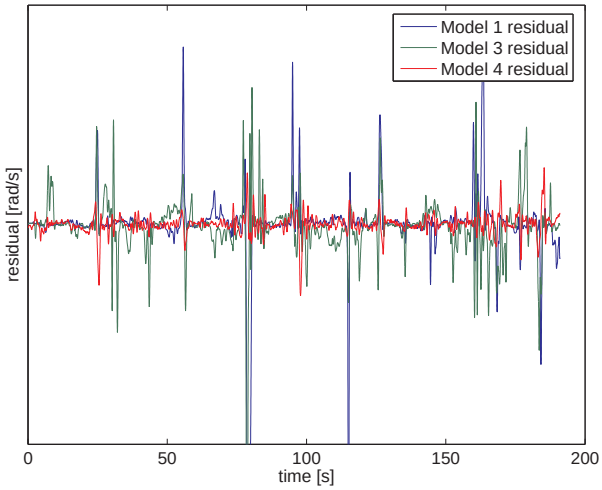

(e) Filtered yaw rate residual.

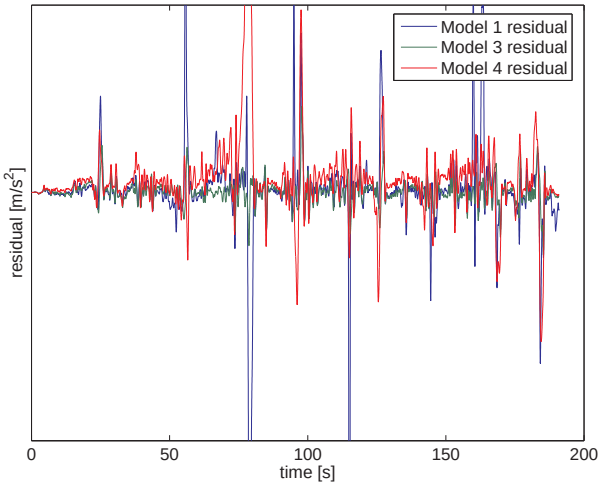

(f) Filtered lateral acceleration residual.

Figure 6.2: Yaw rate and lateral acceleration estimates based on the kinematic models for a handling course maneuver performed on ice.

6.2 Residual filtering

In Figure 6.3(a) the measured and estimated yaw rate are plotted in the same figure. This simulation comes from a test sequence from a handling course maneuver on ice performed in Arjeplog. Figure 6.3(b) is based on the same maneuver but instead depicts the lateral acceleration estimate. In Figures 6.3(c)-6.3(d) the raw residuals are shown and it can be seen that because of model uncertainties they tend to follow the driver input, through steering wheel and gas and brake pedals, to some extent instead of being white noise which would be preferable. In Figures 6.3(e)-6.3(f) these residuals have been high pass filtered according to the method explained in section 5.2.3 and the effects from model uncertainties are no longer detectable.

For the yaw rate, i.e. the leftmost plot, a bias fault of $5°$/s (≈ 0.087 rad/s) has been injected after 50 seconds and the resulting filtered residual can be seen in Figure 6.4(a). Figure 6.4(c) also show the filtered yaw rate residual but here the area around 50 seconds has been magnified and it can be seen that the injected fault gives rise to a large peak in the residual almost instantly and it is thus concluded that this method can be used in order to detect fault in the yaw rate sensor. The short detection time is one of the main advantages with this method. In a similar way Figure 6.4(b) shows the high pass filtered lateral acceleration residual when a bias of 0.5 m/s^2 has been injected after 50 seconds. Also here the fault gives rise to a peak in the residual but it can also be seen that the peak is not as easily distinguishable as was the case for the yaw rate and it is thus harder to detect. This is mainly a result of the high sensor noise levels on the lateral acceleration sensor and this is especially true when driving on ice.

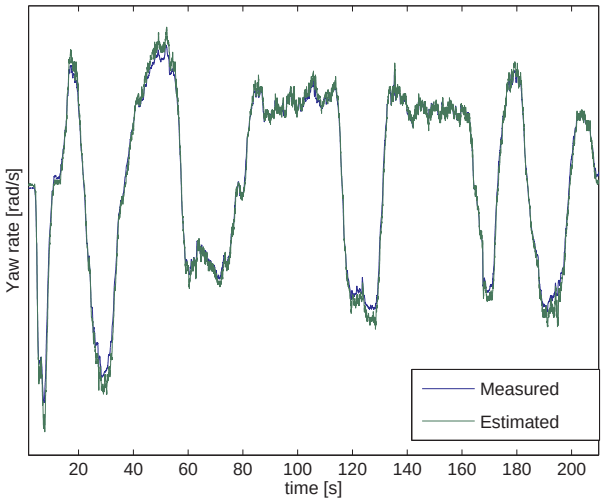

(a) Measured vs. estimated yaw rate.

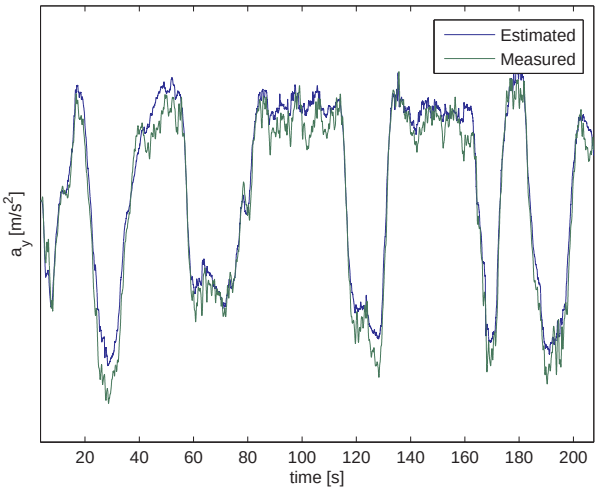

(b) Measured vs. estimated lateral acceleration.

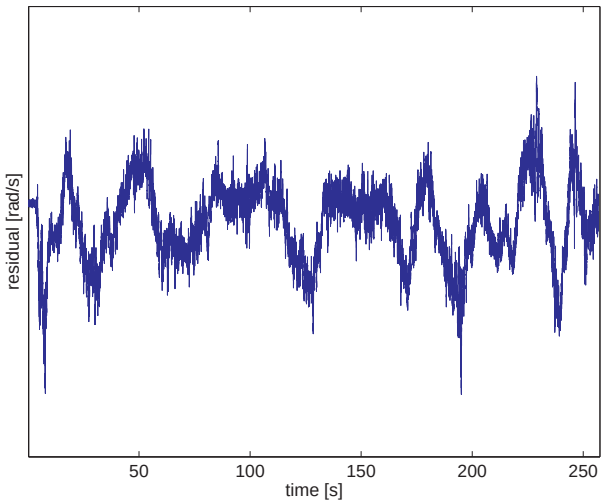

(c) Yaw rate residual.

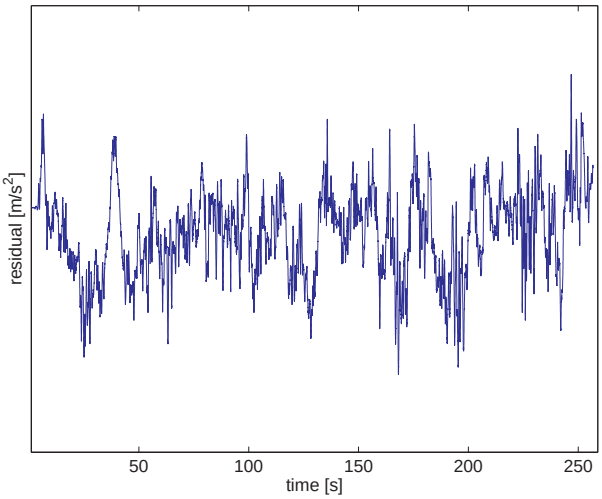

(d) Lateral acceleration residual.

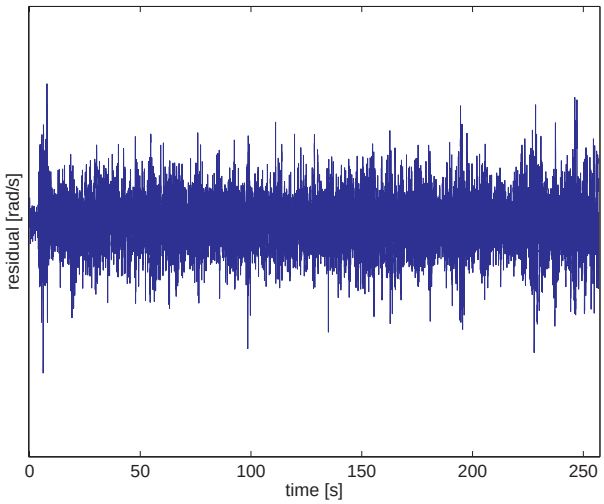

(e) High pass filtered yaw rate residual.

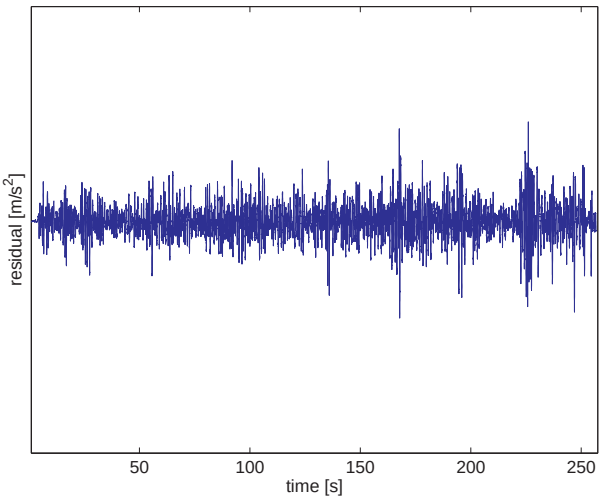

(f) High pass filtered lateral acceleration residual.

Figure 6.3: Yaw rate and lateral acceleration residuals for a handling course maneuver performed on ice.

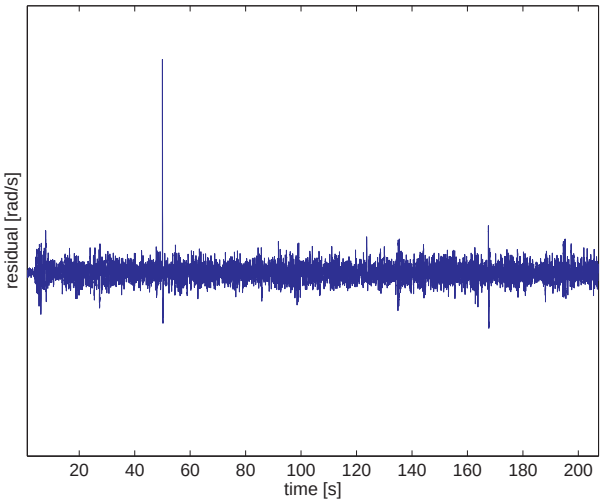

(a) Yaw rate residual with $5°/s$ bias injected after 50 seconds.

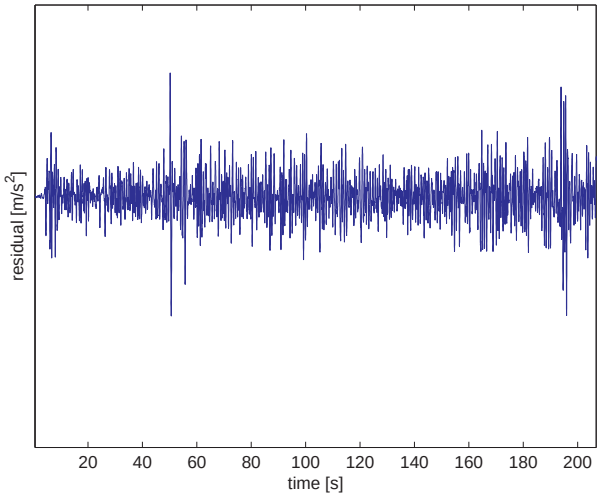

(b) Lateral acceleration residual with 0.5 m/s^2 bias injected after 50 seconds.

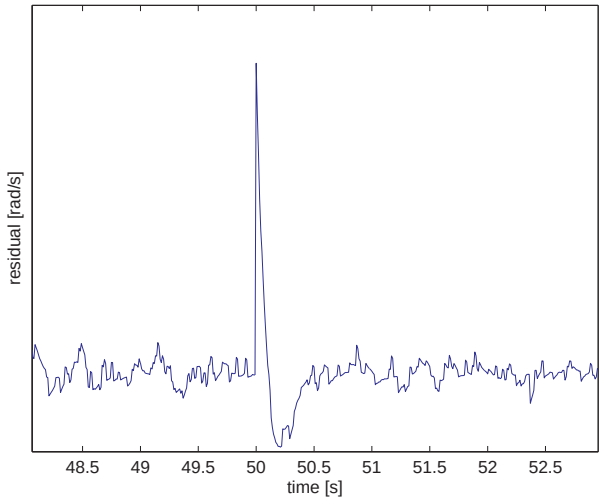

(c) Magnification of the faulted yaw rate residual from Figure 6.4(a).

Figure 6.4: Filtered yaw rate and lateral acceleration residuals for a handling course maneuver performed on ice.

6.3 CuSum

The CuSum algorithm is based on the theory presented in section 5.2.4 and this section will present results from using this method. Two different driving maneuvers are presented and the first is from a slalom maneuver with high lateral acceleration peaks that reach around 9 m/s^2 and where a bias fault has been injected. The second measurement is from an ISO lane change maneuver where a drifting fault has been injected.

For the slalom maneuver, Figures 6.5(a)-6.5(b) show the measured against the estimate of the yaw rate and lateral acceleration respectively while Figures 6.5(c)-6.5(d) show the corresponding, fault-free, residuals. This is a very dynamic driving maneuver and it can be seen that the model is increasingly deteriorating as the lateral acceleration grows. The residuals can be related to the driver input due to model uncertainties rather than having the preferable characteristic Gaussian look. Figure 6.5(e) shows the CuSum test statistic for the yaw rate residual when a bias fault of 5°/s has been injected after 9 seconds. Similarly Figure 6.5(f) shows the test statistic for the lateral acceleration when a fault of 0.5 m/s^2 has been injected after 9 seconds. By studying both test statistics it seems like the fault is not static but rather recurring with a certain frequency. This effect can however be related to the residuals appearances and in this case is related to the turning frequency of the vehicle when performing the slalom maneuver. This is an unwanted effect that arises from model uncertainties.

The following plots are results from performing an ISO lane change maneuver and the CuSum design parameters, h and ν have been chosen to 1 and 0.09 respectively. Figures 6.6(a)-6.6(b) show the measured against the estimate of the yaw rate and lateral acceleration respectively and Figures 6.6(c)-6.6(d) show the corresponding, fault-free, residuals. Here a drift fault has been injected after 9 seconds in both signals. For the yaw rate the drift is 2.5 5°/s and for the lateral acceleration 0.25 m/s^2.

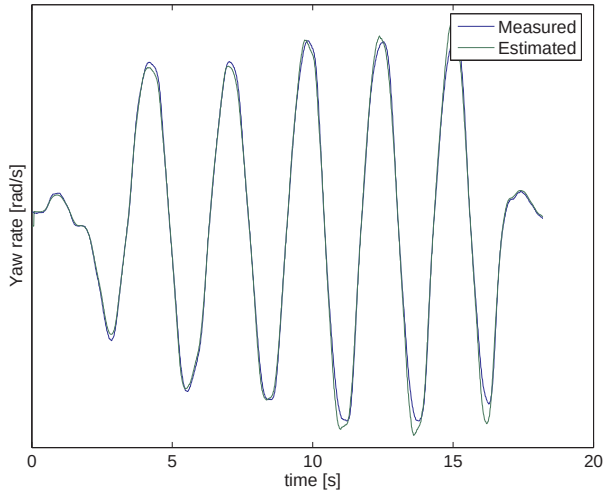

(a) Measured vs. estimated yaw rate.

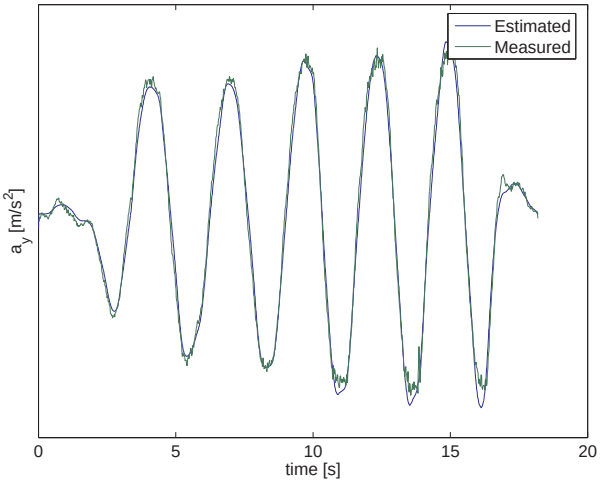

(b) Measured vs. estimated lateral acceleration.

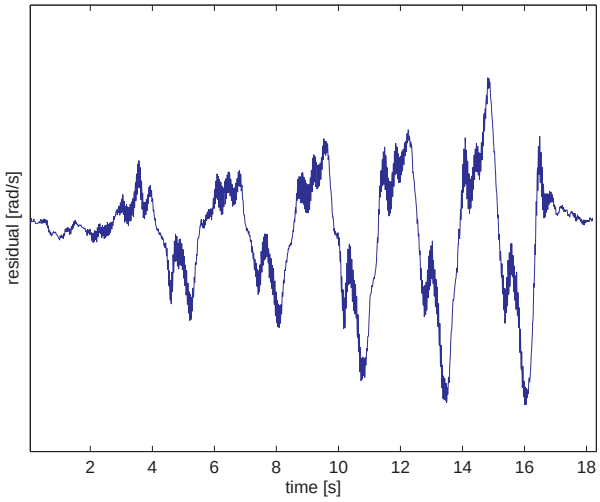

(c) Yaw rate residual.

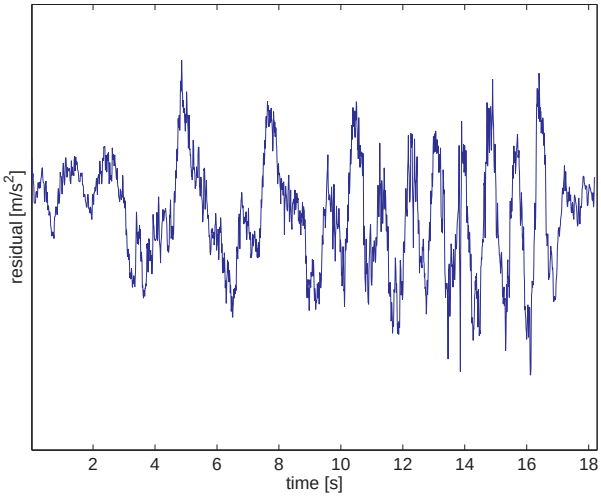

(d) Lateral acceleration residual.

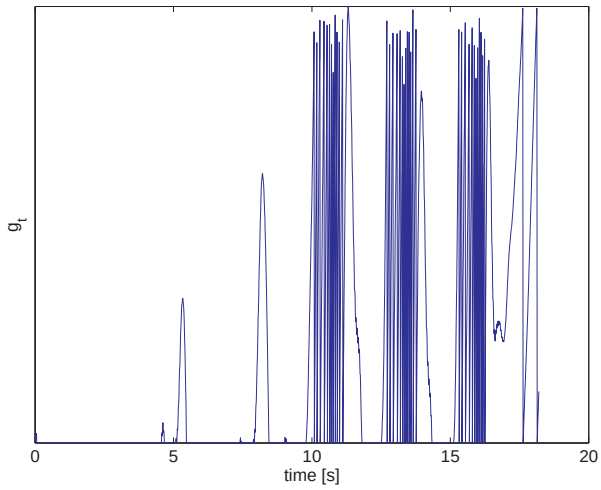

(e) CuSum yaw rate test statistic with a $5^\circ/s$ bias fault injected after 9 seconds.

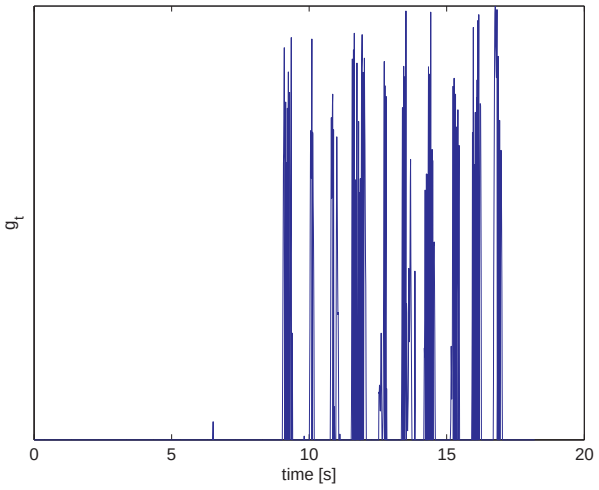

(f) CuSum lateral acceleration test statistic with a 0.5 m/s^2 bias fault injected after 9 seconds.

Figure 6.5: CuSum algorithm behavior for a slalom maneuver performed on asphalt.

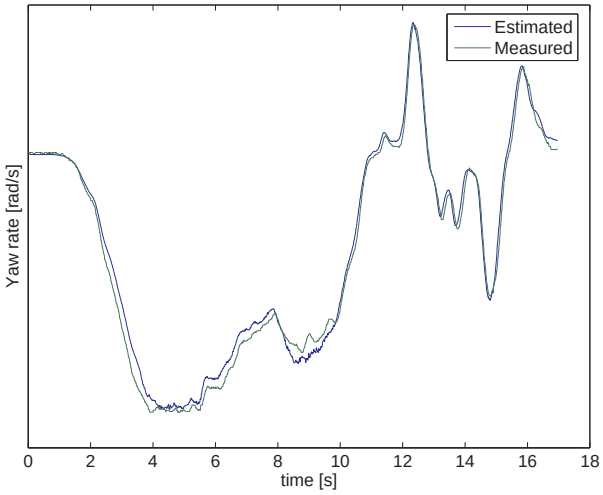

(a) Measured vs. estimated yaw rate.

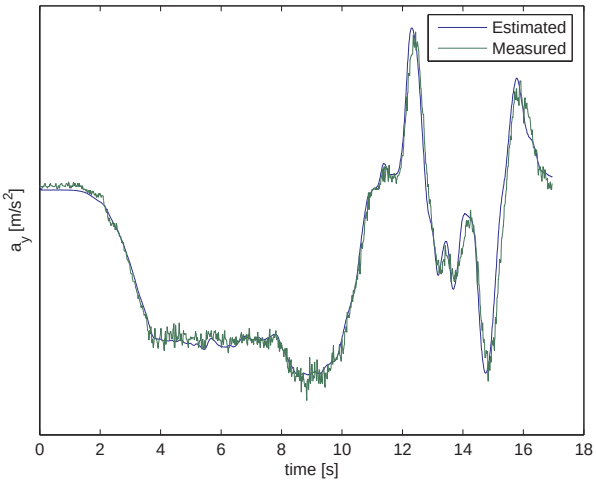

(b) Measured vs. estimated lateral acceleration.

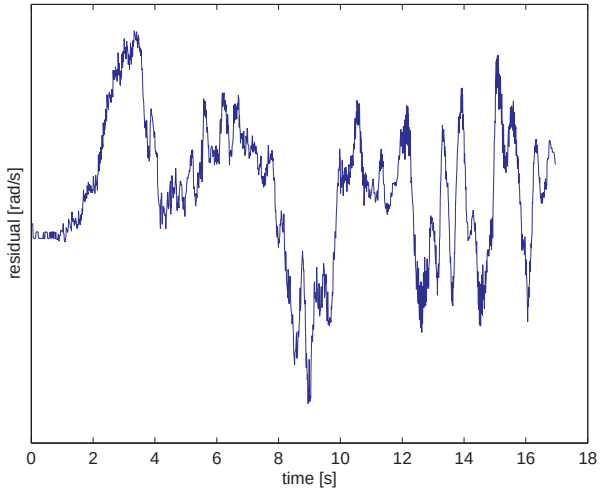

(c) Yaw rate residual.

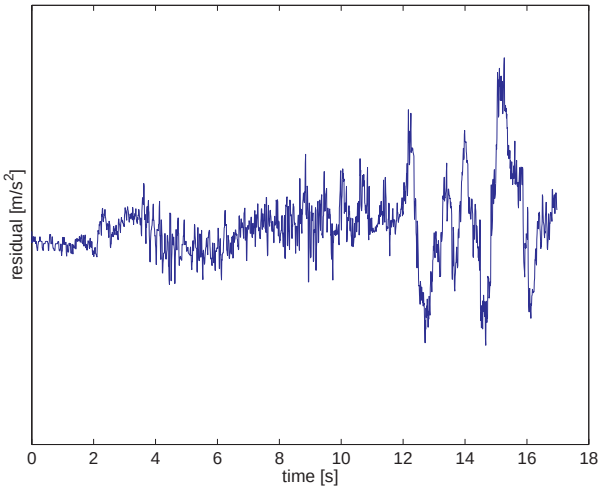

(d) Lateral acceleration residual.

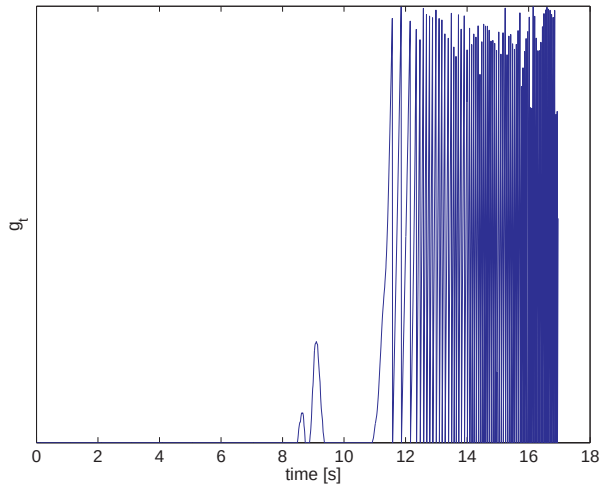

(e) CuSum yaw rate test statistic with a $2.5^\circ/s$ bias fault injected after 9 seconds.

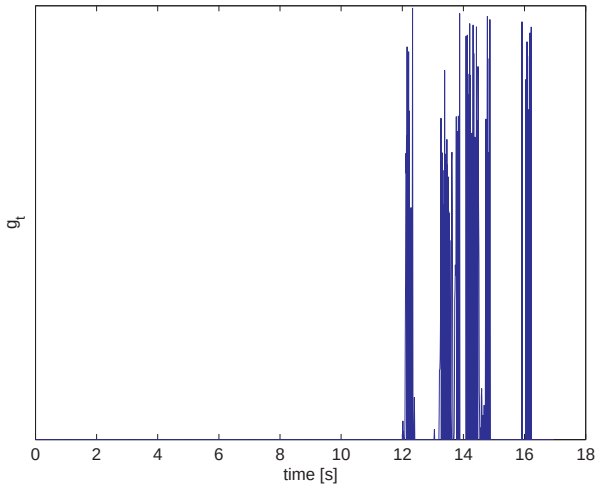

(f) CuSum lateral acceleration test statistic with a 0.25 m/s^2 drift fault injected after 9 seconds.

Figure 6.6: CuSum algorithm behavior for a for an ISO lane change maneuver performed on asphalt.

6.4 Adaptive thresholding

The idea behind adaptive thresholding was explained in section 5.2.2 and in this section the results are presented. This thesis only briefly addresses the area of adaptive thresholding by distinguishing between two different driving modes. In order to display the use of even this simple algorithm Figure 6.7 can be studied. In this figure the yaw rate and the lateral acceleration estimates are shown Figures 6.7(a)-6.7(b) and the respective residuals can be seen in Figures 6.7(c)-6.7(d). The two latter also show the adaptive thresholds. For the yaw rate the lower threshold has been set to 0.12 rad/s and the higher to 0.3 rad/s. The upper level has been determined by not allowing any false alarms for the maneuvers investigated while the lower level has been set by allowing a false alarm rate of 10%. The same goes for the lateral acceleration where the thresholds have been set to 2 and $4\ m/s^2$ respectively. Figures 6.7(e)-6.7(f) also show the thresholded residuals but here a bias fault of 5°/s has been injected into the yaw rate signal and a bias fault of $1\ m/s^2$ has been injected into the lateral acceleratin signal, both after 20 seconds. An important observation is that without the adaptive threshold these faults would not have been detected since the residuals never exceed the upper threshold level.

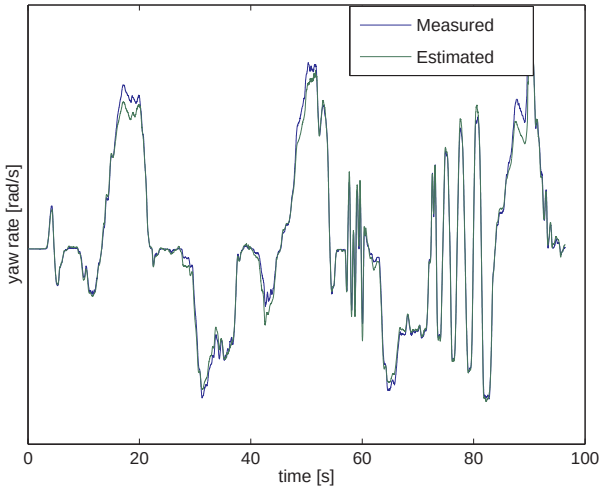

(a) Measured vs. estimated yaw rate.

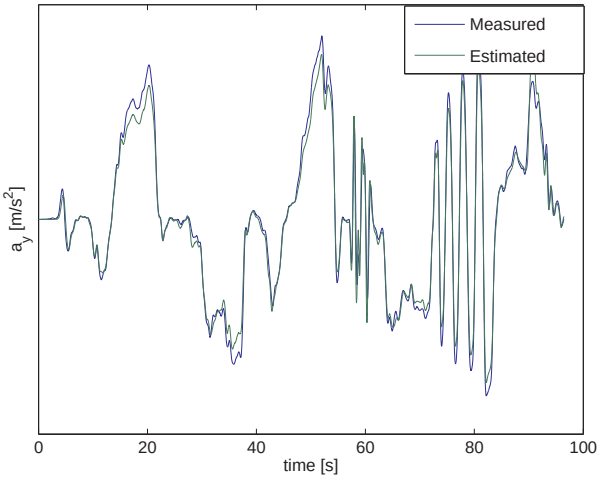

(b) Measured vs. estimated lateral acceleration.

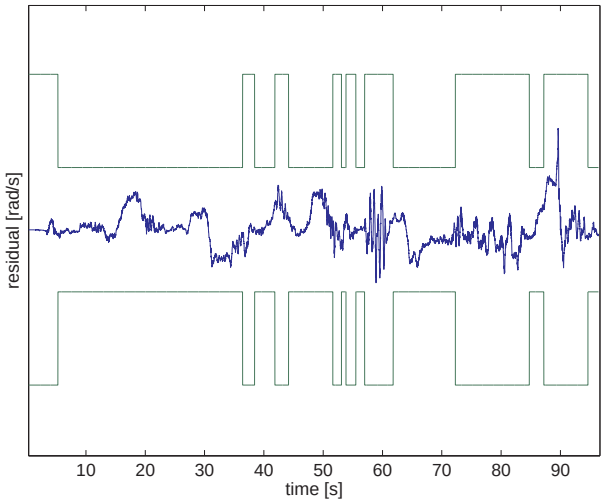

(c) Yaw rate residual together with the adaptive threshold.

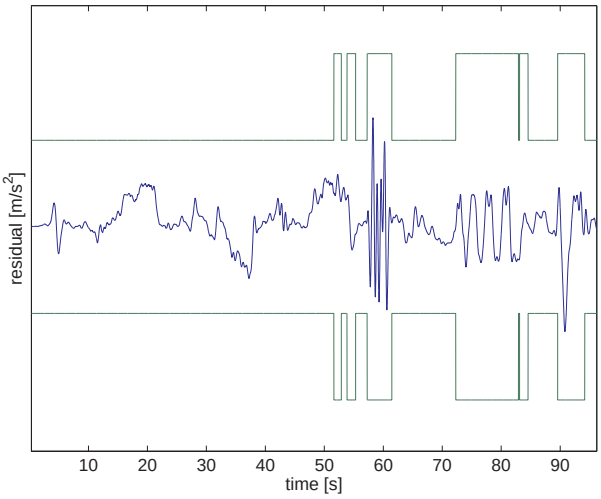

(d) Lateral acceleration residual together with the adaptive threshold.

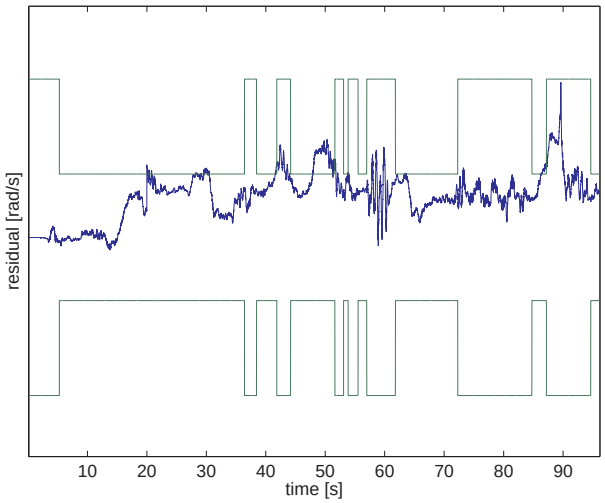

(e) Yaw rate residual together with the adaptive threshold with a $5^\circ/s$ bias fault injected after 20 seconds.

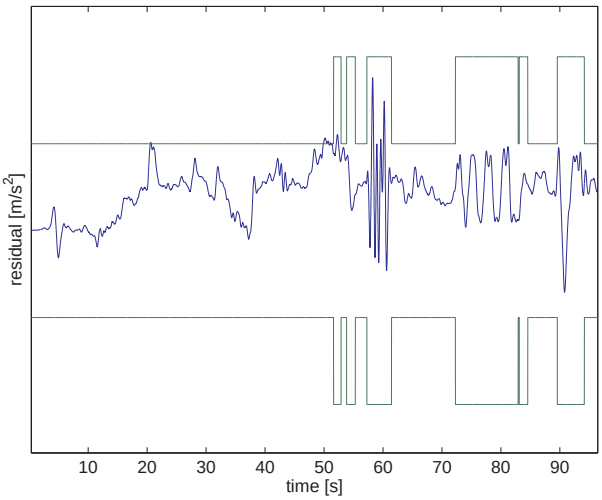

(f) Lateral acceleration residual together with the adaptive threshold with a 1 m/s^2 bias fault injected after 20 seconds.

Figure 6.7: Adaptive thresholding for a handling course maneuver performed on asphalt.

Chapter 7

Conclusions and future work

7.1 Conclusions

The goal with this thesis has been to detect faults in the yaw rate sensor and in the lateral acceleration sensor. First a vehicle model was created and the first approach involved investigating the well known bicycle model. To overcome its main flaws an expansion into a nonlinear two-track model was developed. Important to consider is that no matter how detailed the model is, there will always be model uncertainties arising from uncertainties in parameter estimates, sensor noise and so on. A more accurate vehicle model is of course preferable but it might not improve the performance of the diagnostic system very much. Based on the developed nonlinear model two observers have been designed and used to form residuals as $r = \hat{y}_i - y_i$ in order to observe the yaw rate and lateral acceleration signals. The use of observers renders noise reduction possible and it means that a certain degree of design freedom is possible.

A number of different change detection methods has been investigated in order to detect sensor faults. A fundamental limitation for fault detection schemes is the trade-off between fault detection time and false alarm rate. In vehicular applications it is important to keep the false alarm rate low for safety reasons but at the same time the detection time can not be too large. To find an acceptable balance is one of the biggest challenges in this field. In this thesis a number of common change detection algorithms and methods such as cumulative sum and residual filtering have been investigated. Different methods are investigated to cover the detection of all kind of sensor faults that might occur.

One of the biggest challenges in this thesis lies in the modeling of the vehicle's lateral dynamics. The model derived here provides accurate estimates of both the yaw rate and lateral acceleration as long as the vehicle is not in a "'critical"' driving situation. This introduces different problems, namely to determine what a critical driving situation is and how to determine whether or not the vehicle currently is in this situation or not. A brief investigation into the possibilities of using adaptive thresholding to overcome these problems have been made in order to further optimize the fault detection scheme.

From the results presented in Chapter 6 it can be concluded that the change detection methods investigated can successfully detect faults in both sensors. Residual filtering has been successfully used in order to detect sudden faults in both sensors. The method can however not detect drifting faults and is also very sensitive to measurement noise. The CuSum algorithm provides a more complete method of fault detection that is able to detect all the investigated types of faults. It is also shown how adaptive thresholding renders detection of faults, that otherwise would not have been detectable, possible.

7.2 Future work

Further investigation is possible in several of the fields studied in this thesis. First, improving the vehicle model is one possible way to go. The inclusion of longitudinal forces in the modeling is one way to improve the model accuracy which in this case mainly improves the model behavior during heavy braking and acceleration. It is however important to first evaluate whether or not the diagnosis system will benefit sufficiently from the derivation of a more advanced model or if the time and effort should be spent elsewhere. Furthermore the model can be extended by incorporating the current coefficient of friction to account for various surfaces on-line. A basic framework for inclusion of friction into the model is provided in this thesis but there is room for improvement in

this area mainly by thorough investigation of the tyre forces behavior when driving on various surfaces. Another extension that is possible to make to the model is to include the effects of banked roads. The influence from banked roads has not been investigated in this thesis mainly due to lack of data for driving on banked roads.

Apart from improving the vehicle model, model uncertainties can be handled by more advanced diagnosis schemes and on approach involves the use of adaptive thresholds. The main difficulties here lie within determining what driving situation the vehicle is currently in and the discrete method used in this thesis can be expanded or replaced with more complex methods.

References

[1] A. Andersson. Friction estimation for afs vehicle control. Master's thesis, Lunds Universitet, Lund, Sweden, Juni 2006.

[2] T.D. Gillespie. *Fundamentals of vehicle dynamics*. Society of Automotive Engineers, Inc., 400 Commonwealth Drive, Warrendale PA 15096-0001, 1993.

[3] F. Gustafsson. *Adaptive Filtering and Change Detection*. John Wiley and Sons Ltd, West Sussex, PO19 1UD, England, 2000.

[4] M. Hiemer. *Model Based Detection and Reconstruction of Road Traffic Accidents*. Phd thesis 261, Fakultät für Elektrotechnic und Informationstechnic, Universität Karlsruhe, Universität Karlsruhe, November 2004.

[5] M. Mitschke. *Dynamik der Kraftfahrzeuge, Band C*. Springer Verlag, 1990.

[6] L. Nielsen and L. Eriksson. *Course material Vehicular Systems*. Bokakademin, Linköping, Linköping, Sweden, 2004.

[7] M. Nyberg and E. Frisk. *Model Based Diagnosis of Technical Processes*. Linköping, 2005.

[8] G. Welch and G. Bishop. An introduction to the kalman filter. Technical Report TR95-041, Department of Computer Science, University of North Carolina at Chapel Hill, 1995.

[9] J.Y. Wong. *Theory of Ground Vehicles*. John Wiley and Sons, Inc., 605 Third Avenue, New York, N.Y. 10158-0012, 2001.

Appendix A

Estimated parameters

Bicycle model parameters

Parameter	Notation	Value (asphalt)	Value (ice)	Unit	Comment
Distance between rear axis and CoG	l_r	1.448		m	measured
Distance between front axis and CoG	l_f	1.440		m	measured
Vehicle mass	m	1905		kg	measured

Table A.1: Bicycle model parameters.

Appendix B

Jacobian matrices

The Jacobian matrices consists of all first-order partial derivatives of the nonlinear measurement and differential equations seen in Equation 2.31. The four following Jacobian matrices are therefore required:

$$F_{1,1} = \frac{\partial f_1}{\partial \beta} = \tag{B.1}$$
$$-2\sin\beta\cos\beta\Big\{\beta(\frac{-(C_{\alpha,rl}+C_{\alpha,rr})-(C_{\alpha,fl}+C_{\alpha,fr})\cos\delta_F}{mv_x}) - \frac{\dot{v}_x\tan\beta}{v_x} +$$
$$\dot{\Psi}(\frac{l_r(C_{\alpha,rl}+C_{\alpha,rr})-l_f(C_{\alpha,fl}+C_{\alpha,fr})\cos\delta_F}{mv_x^2} - 1) +$$
$$\delta_F(\frac{C_{\alpha,fl}+C_{\alpha,fr}}{mv_x}\cos\delta_F)\Big\}$$
$$+\cos^2\beta(\frac{-(C_{\alpha rl}+C_{\alpha rr})-(C_{\alpha fl}+C_{\alpha fr})\cos\delta_F}{mv_x}) - \frac{\dot{v}_x}{v_x}$$

$$F_{1,2} = \frac{\partial f_1}{\partial \dot{\Psi}} = \tag{B.2}$$
$$\cos^2\beta(\frac{l_r(C_{\alpha rl}+C_{\alpha rr})-l_f(C_{\alpha fl}+C_{\alpha fr})\cos\delta_F}{mv_x^2} - 1)$$

$$F_{2,1} = \frac{\partial f_2}{\partial \beta} = \tag{B.3}$$
$$\frac{1}{I_z}(l_r(C_{\alpha rl}+C_{\alpha rr}) - l_f(C_{\alpha fl}+C_{\alpha fr})\cos\delta_F + \frac{S_f}{2}(C_{\alpha fr}-C_{\alpha fl})\sin\delta_F)$$

$$F_{2,2} = \frac{\partial f_2}{\partial \dot{\Psi}} = \tag{B.4}$$
$$\frac{1}{I_z}(\frac{-l_r^2(C_{\alpha rl}+C_{\alpha rr})-l_f^2(C_{\alpha fl}+C_{\alpha fr})\cos\delta_F}{v_x} + \frac{S_f l_f}{2v_x}(C_{\alpha fr}-C_{\alpha fl})\sin\delta_F)$$

$$H_{1,1} = \frac{\partial h_1}{\partial \beta} = \tag{B.5}$$
$$-\sin\beta\Big\{\beta(\frac{-(C_{\alpha,rl}+C_{\alpha,rr})-(C_{\alpha,fl}+C_{\alpha,fr})\cos\delta_F}{mv_x}) - \frac{\dot{v}_x\tan\beta}{v_x} +$$
$$\dot{\Psi}(\frac{l_r(C_{\alpha,rl}+C_{\alpha,rr})-l_f(C_{\alpha,fl}+C_{\alpha,fr})\cos\delta_F}{mv_x^2} - 1) + \delta_F(\frac{C_{\alpha,fl}+C_{\alpha,fr}}{mv_x}\cos\delta_F)\Big\}$$
$$+\cos\beta(\frac{-(C_{\alpha rl}+C_{\alpha rr})-(C_{\alpha fl}+C_{\alpha fr})\cos\delta_F}{m}) - \frac{\dot{v}_x}{\cos\beta} + \frac{v_x\dot{\Psi}\tan\beta}{\cos\beta}$$

$$H_{1,2} = \frac{\partial h_1}{\partial \dot{\Psi}} = \tag{B.6}$$
$$\cos\beta(\frac{l_r(C_{\alpha rl}+C_{\alpha rr})-l_f(C_{\alpha fl}+C_{\alpha fr})\cos\delta_F}{mv_x} - v_x) + \frac{v_x}{\cos\beta}$$

$$H_{2,1} = \frac{\partial h_2}{\partial \beta} = 0 \tag{B.7}$$

$$H_{2,2} = \frac{\partial h_2}{\partial \dot{\Psi}} = 1 \tag{B.8}$$

Copyright

Svenska

English